A WIRELESS, MULTI-CHANNEL PRINTED CAPACITIVE STRAIN GAUGE SYSTEM FOR STRUCTURAL HEALTH MONITORING

by

Kshama Lakshmi Ranganatha

A thesis

submitted in partial fulfillment

of the requirements for the degree of

Master of Science in Electrical and Computer Engineering

Boise State University

December 2021

BOISE STATE UNIVERSITY GRADUATE COLLEGE

DEFENSE COMMITTEE AND FINAL READING APPROVALS

of the thesis submitted by

Kshama Lakshmi Ranganatha

Thesis Title: A Wireless, Multi-channel Printed Capacitive Strain Gauge System for Structural Health Monitoring

Date of Final Oral Examination: 04 November 2021

The following individuals read and discussed the thesis submitted by student Kshama Lakshmi Ranganatha, and they evaluated the student's presentation and response to questions during the final oral examination. They found that the student passed the final oral examination.

Benjamin C. Johnson, Ph.D.	Chair, Supervisory Committee
Kurtis D. Cantley, Ph.D.	Member, Supervisory Committee
Zhangxian Deng, Ph.D.	Member, Supervisory Committee
Maria Mitkova, Ph.D.	Member, Supervisory Committee

The final reading approval of the thesis was granted by Benjamin C. Johnson, Ph.D., Chair of the Supervisory Committee. The thesis was approved by the Graduate College.

To my family.

ACKNOWLEDGMENT

This work was supported in part by the National Aeronautics Space Administration under award #80NSSC18M0088.

I am grateful to my advisor, Dr. Benjamin C. Johnson for providing an opportunity to pursue my graduate studies under his supervision. His guidance, patience and constructive discussions have been a crucial part of my graduate studies. I am indebted to him for all the support and encouragement he has provided me during my graduate studies. I would like to thank Dr. Kurtis Cantley, Dr. Maria Mitkova and Dr. Zhangxian Deng for being a part of my supervisory committee.

A very special thanks to my sister and brother-in-law, Sumathi and Adarsh, for supporting and encouraging me through the course of my graduate studies. It wouldn't have been a smooth journey without them. I would like to thank my parents, Ranganath, and Geetha, for all their support, sacrifices and unconditional love. I am truly blessed to have such a wonderful supporting family and I couldn't ask for any better.

Last but not the least, thank you to all my colleagues and friends at Boise State University for all the wonderful memories that will be cherished for the rest of my life.

Kshama Lakshmi Ranganatha

Boise State University

December 2021

ABSTRACT

Structural health monitoring of soft structural textiles plays a key role within the space industry to ensure the safety and integrity of space habitats, parachutes, and decelerator systems. Strain monitoring could be an effective means to evaluate structural integrity, but conventional monitoring systems are not suitable because they are intended for large, rigid structures. To overcome the limitations of rigid sensors, we recently proposed using printed capacitive strain gauges (CSGs) on flexible substrates to monitor the structural health of soft structure materials. Here, we present a strategy and implementation of a wireless, multi-channel readout system for distributed monitoring of soft structural textiles with printed CSGs. The system is comprised of localized sensor motes and a wireless Bluetooth hub. The sensor mote employs a relaxation oscillator frontend to convert capacitance to frequency with a high dynamic range using only three interface wires per mote. The mote's high dynamic range ensures compatibility with various gauge designs and accommodates significant process variation associated with printed gauges. Each hub enables users to read 8 channels of data wirelessly at a sampling rate of 100Hz and can be scaled to higher channel counts through the use of additional hubs. The sensor motes and wireless hub are miniaturized to accommodate flexible substrates, such as a Kevlar strap. The system is tested and exhibits excellent linearity and dynamic range.

TABLE OF CONTENTS

LIST OF TABLES

LIST OF FIGURES

LIST OF PICTURES

LIST OF ABBREVIATIONS

ADC	Analog to Digital Converter
AJP	Aerosol Jet Printing
ATSM	Aluminum Tensile Specimen
BLE	Bluetooth Low Energy
BT	Bluetooth
CSG	Capacitive Strain Gauge
EDL	Entry, Descent and Landing
GF	Gauge Factor
LTP	Lower Trigger Point
MTS	Material Test System
Op-Amp	Operational Amplifier
PZTSG	Piezoelectric Strain Gauge
R-Pi	Raspberry Pi
ROSC	Relaxation Oscillator
RSG	Resistive Strain Gauge
SiC MESFET	Silicon Carbide Metal Semiconductor Field Effect Transistor
SoC	System on Chip
SHM	Structural Health Monitoring
UART	Universal Asynchronous Receiver Transmitter
USB	Universal Serial Bus

UTP	Upper Trigger Point
VTC	Voltage Transfer Curve

CHAPTER ONE: INTRODUCTION

Ensuring the structural health integrity of inflatable space habitats, parachutes, and decelerator systems that use soft structural textiles, also known as softgoods, requires non-invasive testing methods for structural health monitoring (SHM), where high rates of strain are monitored. Soft, flexible materials are utilized over traditional metallic structures to significantly reduce volume and mass. SHM systems are needed to provide emergency notifications to crewmembers in space habitats and enable smart entry, descent, and landing (EDL) operations [1-2]. To do so, a SHM system needs to provide continuous and distributed strain monitoring to detect, diagnose, and locate damage in real time.

Conventional SHM systems are designed for large structures made from rigid materials. However, NASA uses flexible, military-grade Kevlar straps to construct inflatable habitats and parachutes. Ideally, a SHM system would have strain sensors deployed along these 2.54cm-wide straps for comprehensive monitoring. Monitoring the strain of these straps is challenging since conventional strain gauges are stiff, intended for use with metals at low temperatures [1-5]. Recently, we proposed using capacitive strain gauger (CSG) to sense strain on these flexible straps [1]. CSGs are promising alternatives to resistance-based gauges due to higher gauge factors, lower temperature sensitivity, and lack of hysteresis [1]. To fabricate the CSG, our collaborators used aerosol jet printing (AJP) to deposit silver nanoparticles to form interdigitated electrodes on a flexible polymer substrate. AJP can print feature sizes that span from 10μm to 5mm, making it a promising technology for low-cost or in-space manufacturing for SHM [6-7]. Despite excellent

performance and gauge factor, variations in the printing process caused the intrinsic capacitance of the CSGs to vary from pF to nF [1]. Given the constraints of large intrinsic variation, a capacitive interface, and distributed sensing, there is a critical need for a new SHM system.

In this thesis, a wireless, multi-channel readout system tailored to read the change in capacitance from printed CSGs to enable continuous and distributed SHM of soft structural materials. The system demonstrates a sensing architecture for distributed sensing as well as a robust, highly linear readout to accommodate unintentional printed sensor variation.

CHAPTER TWO: STRAIN MONITORING FOR SOFTGOODS

Softgoods

Softgoods are high tensile fabric materials that are known for their flexibility. These materials are engineered to be lightweight and can be used in harsh environments. Due to their flexibility, they are foldable making any deployable structures constructed utilizing them significantly smaller in volume. These textiles have been a popular interest in the space industry ever since the beginning of space exploration as they come with numerous advantages. Picture 1 shows examples of space structures that employ softgoods include extra-vehicular activity (EVA) space suits, satellites, and space habitats (TransHab), [8]. Inflatable structures that employ softgoods have several advantages as they can be carried in a small launch vehicle, easing the process, reducing the cost, and optimizing the internal space of the launch vehicle. Adding to these benefits, the habitat systems are low in mass when compared to traditional rigid structures, which in turn reduces the launching costs. Also, with the use of softgoods, the complexity of the structure reduces, meanwhile increasing the reliability due to very little mechanical components for deployment and other functions of the space habitual systems [8].

Picture 1. EVA Space Suit (left), TransHab (right) [2]

As the lightweight inflatable space structures such as habitats, parachutes, and decelerator systems are constructed using softgoods, testing methods to account for their structural integrity is essential. Common testing approaches such as tensile testing, shear testing and fatigue testing seen in conventional SHM systems designed for large rigid structures like a bridge or an airplane cannot be applied for softgoods [2]. Furthermore, the inflatable structures expand to their final form using pressurized air. Therefore, strain monitoring is essential during this expansion process as it provides vital information of the fabric's structural integrity. Once the structure passes the initial pressure test, continuous strain monitoring is crucial as the safety of the crewmembers is on the line [2]. Thus, a new structural health monitoring system is needed for continuous strain monitoring as it ensures structural integrity of the inflatable space structures and safety of the crewmembers. The new SHM sends emergency notifications for any anomaly detected on the structure that enables smart EDL operations.

Strain Monitoring

Strain is a type of mechanical deformation experienced by the body in the direction of the applied force. In engineering, strain is expressed as the ratio of total deformation to the initial dimension of the material when force is applied, as shown in Figure 2.1, it is also known as Cauchy strain [9]. The mathematical expression for strain is given by the equation 2.1.

$$e = \frac{\Delta L}{L} = \frac{l - L}{L} \tag{2.1}$$

Where,

- e is the strain
- L is the original length of the material
- L is the final length of the material

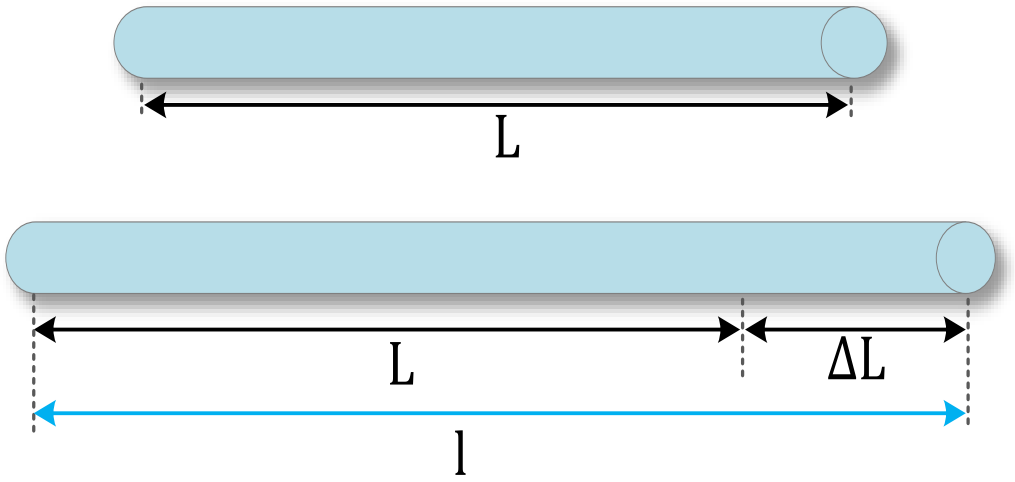

Figure 2.1 Principle of strain

Strain is traditionally monitored through strain gauges. Strain gauge is an electrical sensor whose primary goal is to measure force or strain. There are three types of strain gauges regularly used for strain monitoring.

- Resistive strain gauge (RSG)
- Piezoelectric strain gauge (PZTSG)
- Capacitive strain gauge (CSG)

Resistive Strain Gauge

Resistive strain gauges are the most common gauges used to measure strain. RSGs are made up of long fine wire that form a zig zag pattern whose resistance is given by equation 2.2. As strain is exerted the wire stretches increasing the length and decreasing the cross-sectional area, thus increasing the resistance of the wire [11-12]. This forms the basic principle of the RSG.

$$R = \frac{\rho L}{A} \tag{2.2}$$

Where,

- ρ is the resistivity of the wire
- L is the length of the wire
- A is the cross-sectional area of the wire

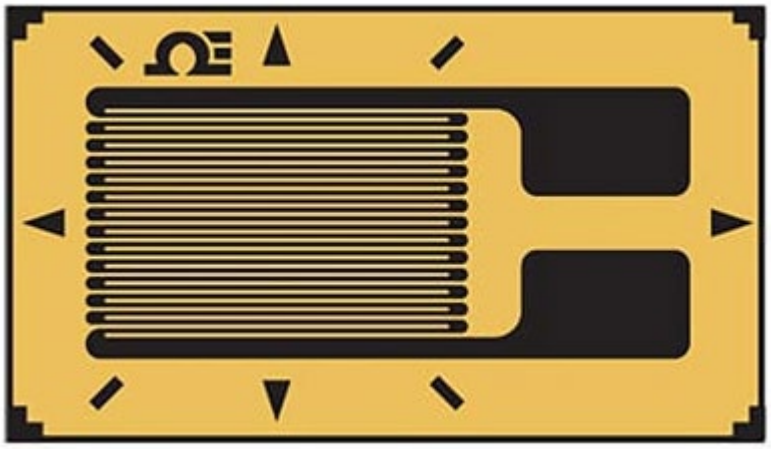

Picture 2. Resistive Strain Gauge [12]

The measuring circuitry involves a Wheatstone bridge structure as seen in Figure 2.2. The resistance of the strain gauge is given by equations 2.3 and 2.4 following the principle of Wheatstone bridge. Therefore, as the strain increases, the resistance increases and vice versa.

$$\frac{R_2}{R_1 + R_2} = \frac{R_S}{R_S + R_3} \tag{2.3}$$

$$R_S = \frac{R_2 R_3}{R_1} \tag{2.4}$$

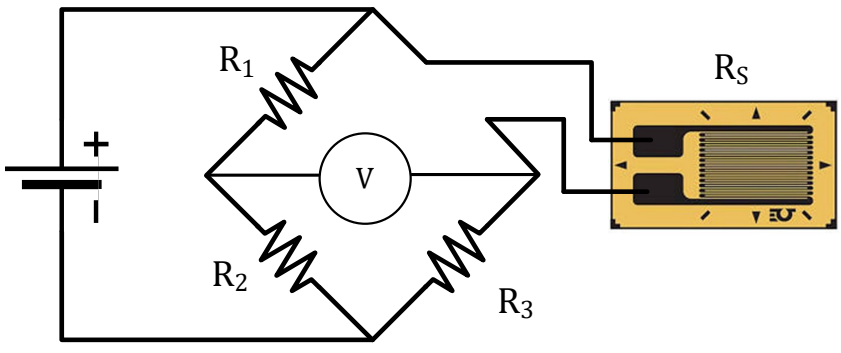

Figure 2.2 Wheatstone Bridge Structure [10]

The sensing resolution of the strain gauge is given by gauge factor (GF) [12]. Gauge factor is the ratio of the resistance change to the mechanical strain that is expressed in equation 2.5.

$$GF = \frac{\frac{\Delta R}{R}}{e} \tag{2.5}$$

Where,

- e is the strain

RSGs can be used on any solid material or even embedded into cement, as they have stiff substrates [10]. They are popular due to their ability to rapidly track varying strain. However, they mostly operate at room temperatures. They are prone to device failure in long term testing and are sensitive to temperature. Their inherent stiffness results in device failure under high loads. Their temperature sensitivity leads to hysteresis and non-linearity with respect to strain in their performance as the gauge factor does not remain constant. Most RSG can tolerate at most 5% of strain [1]. Manufacturing RSG is a complex and exhaustive process leading to high material waste and fabrication cost.

Piezoelectric Strain Gauge

Piezoelectric strain gauges (PZTSG) follow the principle behind piezoelectricity where mechanical energy is converted to electrical energy. They generate voltage when strain is applied. They exhibit excellent sensitivity making them highly reliable [14-15]. These sensors are known to consume lower power and their charge output lies in the measuring range of commercially available analog or digital sensors. They exhibit high gauge factor in the range of 20 or higher and find popular interest in the flexible electronics community for wearable sensor applications. They also overcome the hysteresis problem of RSGs as they can operate at higher temperatures. The measurement systems for PZT

strain sensors usually employ a power amplifier with various excitation signals with varying frequencies.

Capacitive Strain Gauge

CSGs are very robust as they overcome the hysteresis issue of RSGs. They employ electrodes in their design and are highly dependent on geometric changes between electrodes and dielectric layers that do not suffer permanent damage in cyclic testing [1]. There are two types of CSGs:

- Parallel plate CSG
- Interdigitated electrode CSG

Commercially available CSGs employ the parallel plate design exhibiting a gauge factor range of 15-30. They show low sensitivity to noise and temperature. But their use is restrictive as it is difficult to measure strain in the direction that is perpendicular electrode alignment and are limited to the structures. Also, parallel plate CSGs require bulky electromechanical devices for mechanical attachment onto structural components [1].

In comparison to the parallel plate design, the interdigitated electrode design has been experimentally proven to withstand harsh environments and provide a means to directly attach onto structural components such as Kevlar straps [1]. Studies have concluded that using CSGs is highly suitable for wireless applications. These advantages of CSGs have led to in-depth research in optimizing their performance by various printing processes.

Therefore, interdigitated electrode CSG poses a suitable candidate to be used for strain monitoring of softgoods. With recent advancements in additive manufacturing

methods such as aerosol jet printing (AJP) highly flexible printed electronics can be fabricated [1]. Thus, an interdigitated electrode AJP strain sensor is discussed in detail.

Aerosol Jet Printed CSG

AJP technology is a non-contact deposition method based on atomization of inks to form aerosols pre-deposition onto the substrate. Here, the printed device is fabricated using a functional material in nanoparticle form that is deposited onto a flexible polymer substrate [1]. The ability of AJP to atomize ink to form aerosol facilitates a wide range of surfaces for deposition and a wide range of feature size spanning between 10μm to 5mm. Once the device is fabricated it can be directly attached onto any surface from solid surfaces such as metal to flexible materials such as softgoods. Additionally, AJP paves the way to use the sensors on any surface unlike the parallel palate CSG and have low manufacturing cost [1]. Hence, AJP flexible CSG intended for the use with softgoods to aid SHM of the inflatable structure is presented below.

The aerosol jet printed CSGs were fabricated using silver nanoparticle ink on a flexible polymer substrate. These CSGs employ interdigitated electrode structure designs that act as multiple parallel plate capacitors in series [1]. To accommodate copper leads of the CSGs, silver epoxy was used along with poly methyl methacrylate (PMMA) acting as both the protective covering and the dielectric between electrodes. The PMMA layer has a uniform thickness of 10.2 ± 0.1μm making it an effective way to encapsulate the digits. The said CSG was printed on a Kapton substrate. The distance between the copper leads has two main contributing factors that is (i) extension of the fabric and (ii) extension of the Kapton substrate. With some meticulous calibration between the Kevlar strap and Kapton substrate, an electrical result in the form of varying capacitance can be determined.

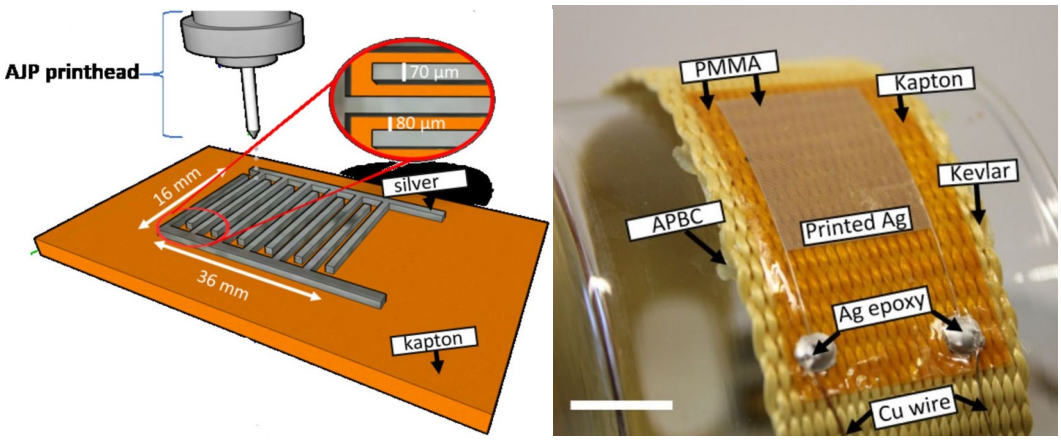

Figure 2.3 Design of printed flexible interdigitated electrode capacitive strain gauge [1]

To construct inflatable habitats and parachutes, NASA uses military grade Kevlar straps that are 2.54cm wide and are a type of softgoods that are known to withstand heavy loads [2]. Therefore, the CSGs were attached onto the Kevlar straps by all-purpose barge cement (APBC) [1]. The fabricated sensor as seen in Figure 2.3, with the components discussed above spans 3.6cm and 1.6cm with a total of 100 electrodes.

The theoretical resting capacitance C_0, and theoretical strained capacitance of the CSGs are calculated from equations 2.6-2.8 in [16-17].

$$C_0 = pt(2l - a + 2w)\left(\frac{2n-1}{d}\right)\varepsilon_0 \tag{2.6}$$

$$C_{perpendicular} = pt(1-ve)\big((1-ve)(2l - a + 2w)\big)\left(\frac{2n-1}{d(1+e)}\right)\varepsilon_0 \tag{2.7}$$

$$C_{parallel} = pt(1-ve)\big((1+ve)(2l - a + 2w)\big)\left(\frac{2n-1}{d(1-e)}\right)\varepsilon_0 \tag{2.8}$$

Where,

- p is the dielectric constant of PMMA
- t is the thickness of the printed silver digit

- l is the length of the digit
- a is the total width of the interdigitated electrodes
- w is the width of the digit
- n is the number of digit pairs
- e is the strain in the sensitive axis of the strain sensor
- ε_0 is the permittivity of free space
- d is the distance between electrodes

Substituting the dimensions of the printed CSGs from table 2.1 into equations 2.7 and 2.8, the intrinsic capacitance was expected to fall in the range of 4.56pF to 6.70pF. But the measured intrinsic i.e., resting capacitance was in the range of 42pF to 15nF. This wide deviation is due to variations in the printing process that leads to the formation of bulbous structures at the end of electrodes. Regardless of this, the strain sensor exhibits excellent performance when subjected to 70% of maximum rated load for Kevlar strap of 26.7kN i.e., 18.7kN where the strap experienced an average strain of 0.060 ± 0.001 and the calculated gauge factor was 5.2 [1].

Table 2.1 Design Parameters for Printed CSG

Paramete	Value
p	5.7
t	2.7 ± 0.2µm
l	15.74 ± 0.02µm
a	16.07 ± 0.01µm
w	71 ± 4µm
d	78 ± 3 µm
n	50
ε_0	8.8542×10^{-12} F/m

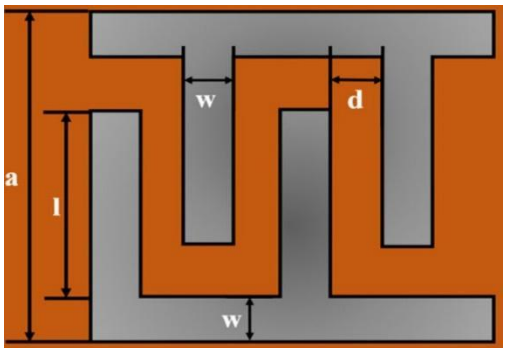

Figure 2.4 CSG Interdigitated electrode structure detailing design parameters [1]

Incorporating the AJP flexible CSG for SHM of inflatable structures, a high dynamic range readout system is required for continuous strain monitoring. This system should be capable of handling distributed strain sensing, as there are multiple strain sensors deployed on the inflatable structures' Kevlar straps. Though the printed CSGs provide excellent performance and sensitivity, a readout system that facilitates the capacitive interface and the large intrinsic capacitive variation is essential. Additionally, the SHM system should enable distributed strain sensing that is easy to assemble, low cost and sizable to Kevlar straps. Therefore, a highly linear and high dynamic range readout system is discussed in this chapter that lays the foundation for a new SHM system for inflatable space structures. Furthermore, to avoid any entanglement of cables associated with the readout system, the design and verification of a wireless sensing system with minimal associated wiring is discussed in the next chapter.

CHAPTER THREE: WIRELESS, MULTI-CHANNEL PRINTED CSG SYSTEM FOR SHM

To facilitate the use of multiple AJP flexible CSG sensors for distributed sensing, and fast data acquisition, a wireless, multi-channel system is designed for SHM of inflatable structures, that is conceptualized in Figure 3.1.

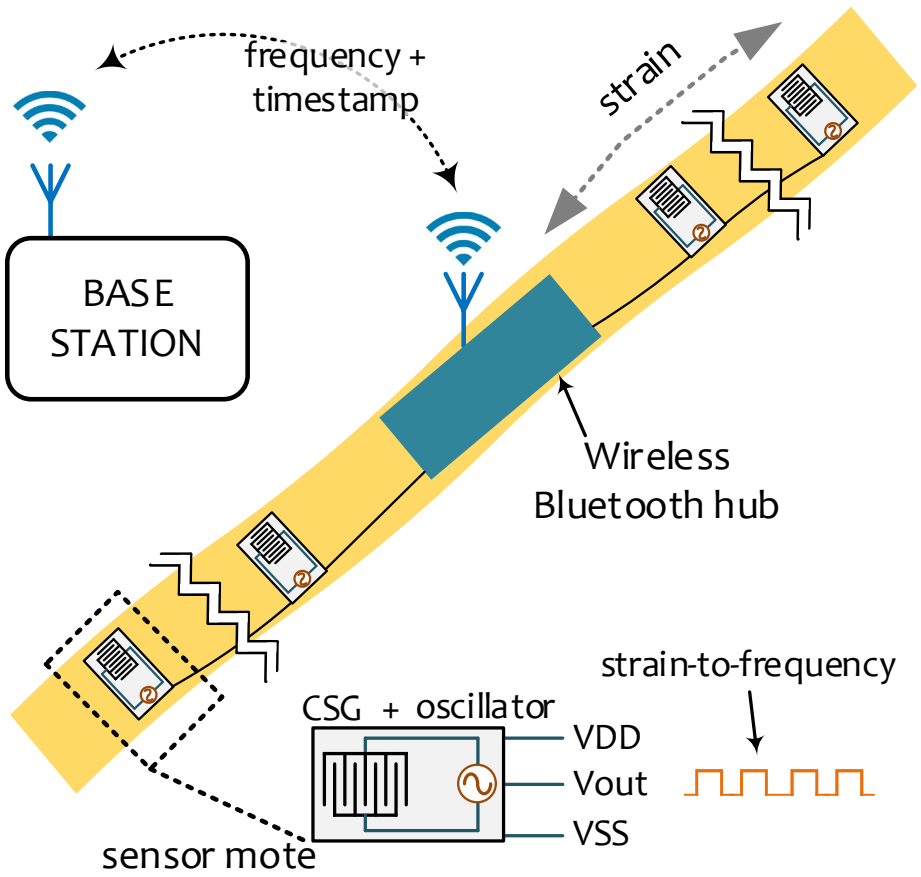

Figure 3.1 Concept of Wireless Multi-Channel CSG System

Here, the system consists of multiple sensor motes where the outputs of these motes are attached to a wireless hub. Each sensor mote encompasses a CSG and a relaxation

oscillator. The oscillator's frequency is set by the CSG capacitance. As the Kevlar strap is strained, the capacitance of the CSG changes thereby changing the oscillator's output frequency. As the frequency changes, a counter on the microcontroller of the hub is enabled that determines the frequency by counting the oscillation pulses within a set programmable window. The programmable window calibrates the trade-off between the sampling rate of the counter and the dynamic range of the frequency readout. The implementation and assembly of the sensor mote and wireless hub of the presented SHM system concept is discussed in the following sections below.

Sensor Mote

Efficient and scalable capacitive readout of the printed CSG sensor present a few challenges. Firstly, unlike resistive gauges, CSGs cannot utilize the commonly used DC signal enabled Wheatstone bridge method that is used for RSGs to determine the capacitance variation with respect to the applied strain [18]. At the system level, this would mean measuring the voltage change (eq. 3.1) by generating multiple current signals. Alternatively, it would imply measuring complex impedance (eq. 3.2) by generating multiple sinusoidal signals. Secondly, the AJP CSGs exhibit a wide range of intrinsic capacitance between 42pF to 15nF. As discussed in the previous chapter, this is due to variations in the printing process of the CSG but does not interfere with the sensor performance altogether. Therefore, this broad intrinsic capacitance range is difficult to gauge using conventional readout circuitry as they are designed for very small capacitance in the range of a few pF [8-21]. The conventional readout systems include:

- Amplitude Modulation
- Clapp-Type Oscillator

- Capacitive Coupled Amplifier

$$i = C \cdot \frac{dV}{dt} \tag{3.1}$$

$$Z_C = \frac{1}{j\omega C} \tag{3.2}$$

Where,

- *dV/dt* is the rate of change of voltage
- *C* is the capacitance
- ω is the frequency of the sinusoidal signal

Amplitude Modulation

The amplitude modulation readout scheme is based on the principle of modulating the output voltage with respect to the changing capacitance value where the transfer function is given by equation 3.3 [21]. This readout circuit, referred to Figure 3.2, comprises of a reference capacitance C_{ref}, a buffer, sensor capacitance C_x and a transmitting antenna. Using the buffer whose gain is set to one avoids any coupling that might occur due to the reference capacitance and the parasitic capacitance that is outside the circuit. The output of the transmitter is a modulated sinusoidal signal that corresponds to sensor capacitance C_x and the input sine wave V_{in}. As the reference capacitance is a constant value, the output voltage increases as the sensor capacitance increases. This voltage is transmitted and received by an external receiver that is later analyzed using an oscilloscope [21].

$$V_{out} = \frac{C_x}{C_x + C_{ref}} \cdot V_{in} \tag{3.3}$$

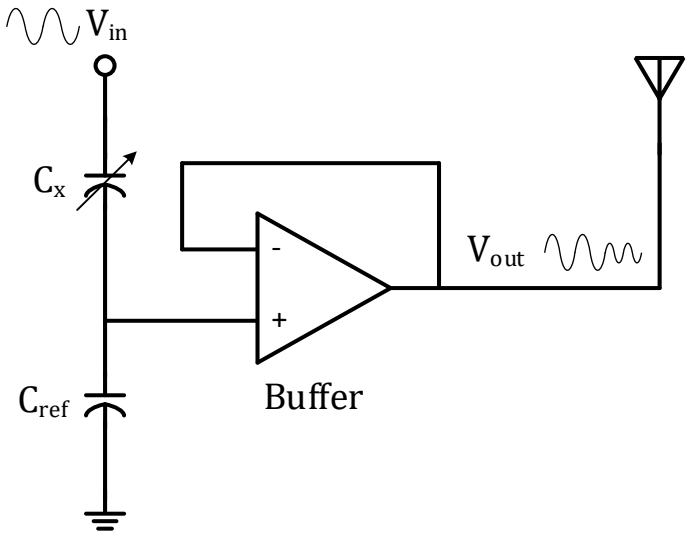

Figure 3.2 Amplitude Modulation for Capacitive Sensing

Clapp-Type Oscillator

The Clapp-type oscillator design uses a Silicon Carbide metal semiconductor field effect transistor (SiC MESFET) whose oscillation frequency is set by equation 3.4 [22-23]. This circuit, seen in Figure 3.3, is used as a variable oscillator where the capacitor sensor is placed in series with the tank circuit inductor L_T. But this circuit can be used for operation with fixed frequencies thereby limiting the range of acceptable capacitance range of the sensor [22-23].

$$f_{Co_{osc}} = \frac{1}{2\pi\sqrt{L_T C}} \tag{3.4}$$

$$\frac{1}{C} = \frac{1}{C_1} + \frac{1}{C_2} + \frac{1}{C_D} + \frac{1}{C_S} \tag{3.5}$$

Where,

- $f_{Co_{osc}}$ is the oscillation frequency of Clapp-type oscillator
- L_T is the inductor of the tank circuit
- C is the total capacitance

- C_S is the tank capacitance

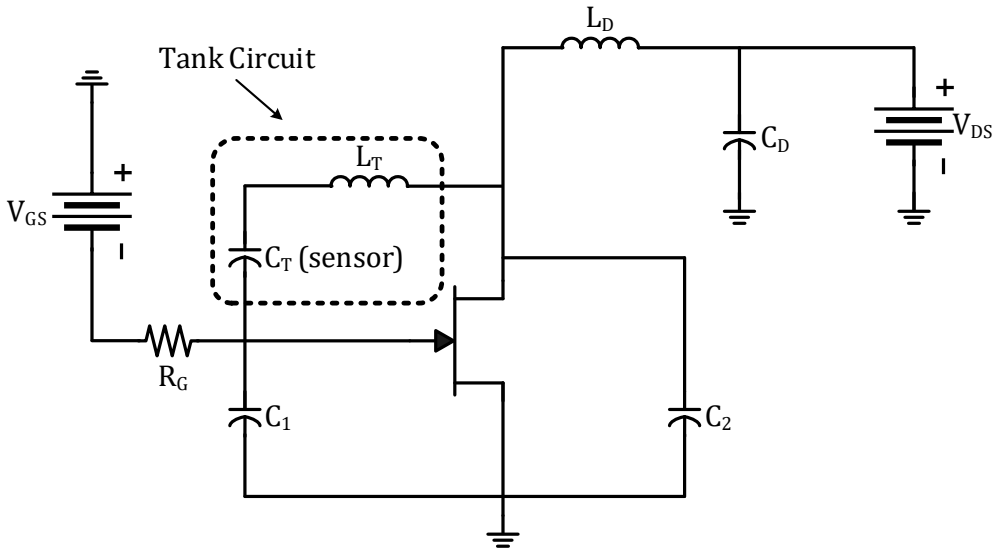

Figure 3.3 Clapp-Type Oscillator for Capacitive Sensing

Capacitive Coupled Amplifier with Peak Detector

The capacitive coupled amplifier design employs an operational amplifier with a parallel resistor and capacitor feedback network as seen in Figure 3.4. The transfer function of this readout circuit is given by equation 3.6. From the transfer function we can infer that the output of amplifier is directly correlated to the input voltage, V_{in}, and the sensor capacitance C_S. The peak voltage of the output is accounted for by the Peak detector that consists of a diode and a capacitor. The peak voltage, V_{peak} is given by equation 3.7.

$$V_p = V_{in}\frac{C_S}{C_{fb}} \tag{3.6}$$

$$V_{peak} = V_p - 0.7 \tag{3.7}$$

Where, 0.7V is the voltage drop across the diode.

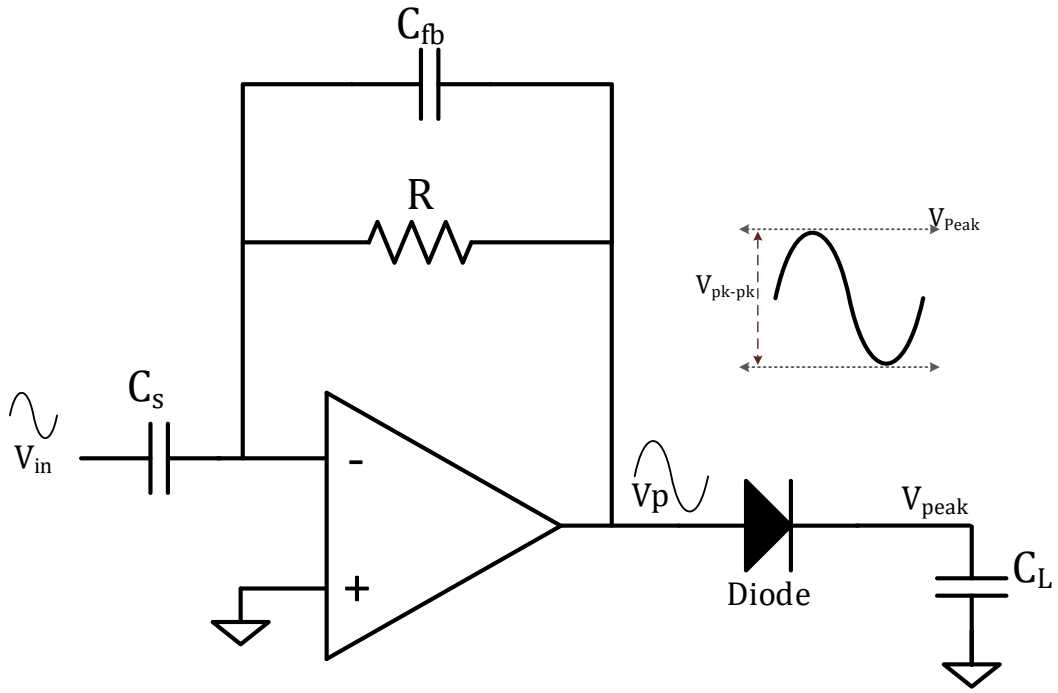

Figure 3.4 Capacitive Coupled Amplifier with Peak Detector

Although the above approaches have proven to have excellent performance to accommodate capacitive sensors, the issue lies with the requirement of additional excitation signals and voltages. The amplitude modulation circuit and the capacitive coupled amplifier circuits require a sinusoidal signal that require additional complex circuit elements that would not be sizable to the Kevlar strap. The Clapp-type oscillator design requires additional voltage source and bulky inductors, and it is limited in the range of acceptable frequency therefore, making it difficult to calibrate to the intrinsic capacitance range of the CSG. Thus, a relaxation oscillator that employs capacitance-to-frequency readout scheme is chosen for the sensor mote circuit as it eliminates the need for additional sinusoidal signals, voltages, and bulky inductors, and limiting the number of connecting cables to the wireless hub to three. The relaxation oscillator used employs an inverting Schmitt trigger with resistive feedback that outputs a digital clock that is linearly dependent on the input capacitance.

Relaxation Oscillator

Relaxation oscillator (ROSC) is a non-linear oscillator that provides a non-sinusoidal recurring output waveform such as a triangular or square waveform. The circuit design involves an energy storing device such a capacitor that charges or discharges continuously. Thus, the output frequency of the circuit depends on the time constant of the capacitive circuit. There are several topologies of the ROSC. The most known ROSC topologies consist of an inverting Schmitt trigger and a RC circuit. There are two types of Schmitt trigger-based ROSC topologies:

- Analog: Inverting Schmitt trigger ROSC
- Digital: Schmitt trigger inverter ROSC

Analog: Inverting Schmitt Trigger ROSC

The analog inverting Schmitt trigger consists of an operational amplifier(op-amp) that is used as a threshold comparator with a resistive network as seen in Figure 3.5. The threshold voltage is set by the non-inverting input of the op-amp and then compared to the inverting input voltage [24]. For an inverting Schmitt trigger, there are two trigger points known as upper trigger point (UTP) and lower trigger point (LTP). This is set by the voltage drop across the resistor R_1 with respect to the change in input voltage at the inverting terminal [24]. This fundamental principle is given below.

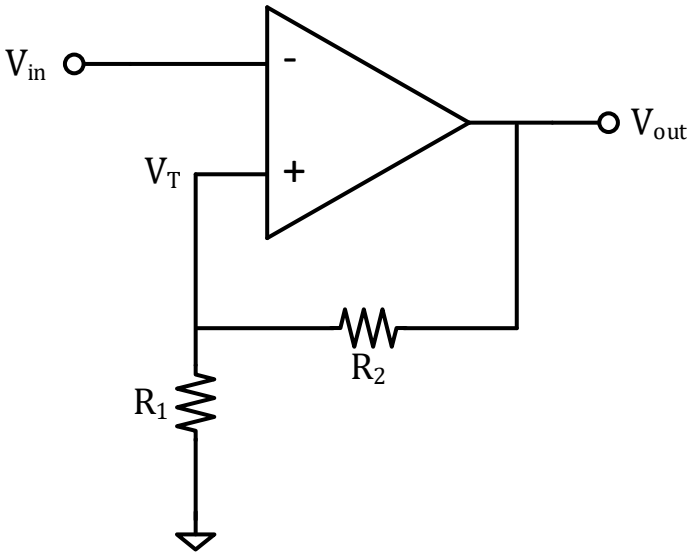

Figure 3.5 Inverting Schmitt trigger

Initial conditions are set by:

$$V_{in} = -V_0 \rightarrow V_{out} = V_0;$$

Where, V_0 is the maximum output voltage of the op-amp

The threshold voltage at the non-inverting terminal is given by:

$$UTP = V_T = V_o \left[\frac{R_1}{R_1 + R_2}\right] \tag{3.8}$$

V_{in} should rise above the threshold value V_T to change V_{out} state at which point,

$$V_{out} = -V_0;$$

$$LTP = -V_T = -V_0 \left[\frac{R_1}{R_1 + R_2}\right] \tag{3.9}$$

V_{in} should now go to a lower value to change the state of V_{out}.

The input/output characteristics often referred to as voltage transfer curve (VTC) in the digital IC domain gives the relationship of the output with respect to the input. An inverting Schmitt trigger, the VTC displays hysteresis, which occurs due to the difference of UTP and LTP. The benefitting effect of hysteresis of this circuit is elimination of noise

triggers. Figure 3.6 illustrates this hysteresis curve followed by the detailed explanation [24].

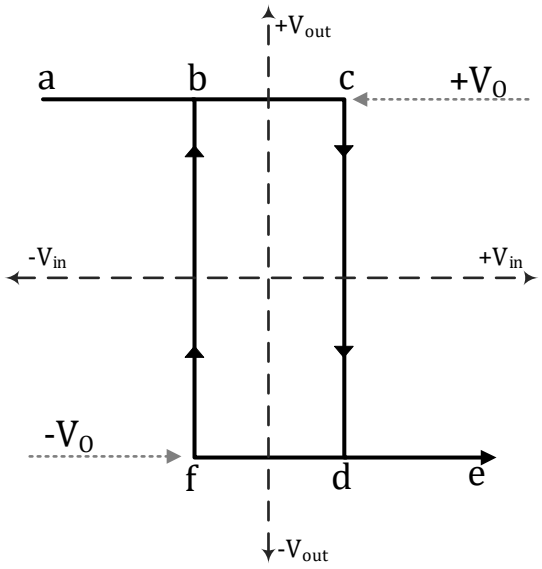

Figure 3.6 Schmitt trigger hysteresis

Explanation of the hysteresis curve:

- At a, $V_{out} = +V_o$; and $V_{in} < LTP$ therefore, $V_{out} = +V_o$
- At a through b and c, V_{in} is increased from LTP until it reaches UTP, $V_{out} = +V_o$
- From c to d, V_{out} swiftly switched from $+V_o$ to $-V_o$ as $V_{in} = UTP$
- From d to e, $V_{out} = -V_o$ as V_{in} is above UTP
- At e through d and f, $V_{out} = -V_o$ as V_{in} is reduced from UTP until it reaches LTP
- From f to b, V_{out} is swiftly switched to $+V_o$ from $-V_o$ as $V_{in} = LTP$
- From b to a, $V_{out} = +V_o$ as $V_{in} < LTP$

When the inverting Schmitt trigger is combined with a RC delay, we get an oscillation output. This circuit is known as relaxation oscillator, as seen in Figure 3.7. The

output of the ROSC is a digital clock signal [24]. The oscillation period of the ROSC is derived below.

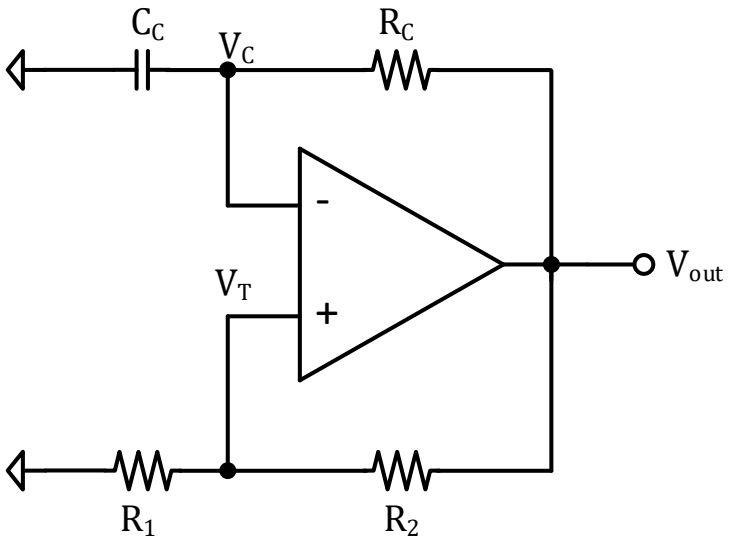

Figure 3.7 Op-amp based relaxation oscillator

Define boundary conditions at node V_c

$$V_C(0) = -V_T$$

$$V_C(\infty) = V_o$$

Therefore,

$$V_C(t) = V_0 - [V_0 + V_T]e^{-\frac{t}{R_C C_C}} \tag{3.10}$$

Solving equation 3.10 at T/2:

$$V_C\left[\frac{T}{2}\right] = V_0 - [V_o + V_T]e^{-\frac{T}{2R_C C_C}} = V_T \tag{3.11}$$

Therefore,

$$T = -2R_C C_C \ln\left[\frac{V_o - V_T}{V_0 + V_T}\right] \tag{3.12}$$

$$T = 2R_C C_C \ln\left[\frac{V_o + V_T}{V_0 - V_T}\right] \tag{3.13}$$

Substituting UTP and LTP from equations 3.8 and 3.9:

$$T = 2R_C C_C \ln\left[\frac{1 + \frac{R_1}{R_1 + R_2}}{1 - \frac{R_1}{R_1 + R_2}}\right] \tag{3.14}$$

$$T = 2R_C C_C \ln\left[\frac{2R_1 + R_2}{R_2}\right] \tag{3.15}$$

Digital: Schmitt trigger inverter ROSC

In digital IC design the Schmitt trigger inverter gate is a logic gate that is designed for arithmetic and logical operations. The logical operation behind a Schmitt trigger inverter is like that of an inverter as seen in Table 3.1. Commonly, this logic gate is built using NAND gates or inverters [25]. A simple Schmitt trigger circuit is made up of four inverters as seen in Figure 3.8a where the inverter in the feedback circuit sets the trigger points also known as switching thresholds, V_{th+} and V_{th-}, that gives rise to hysteresis referred to Figure 3.8c. These circuits have the ability to interpret input voltage change according to the switching threshold values. The circuit eliminates the need for the resistor network as seen in its analog counterpart.

Table 3.1 Schmitt trigger inverter truth table

A	Y
1	0
0	1

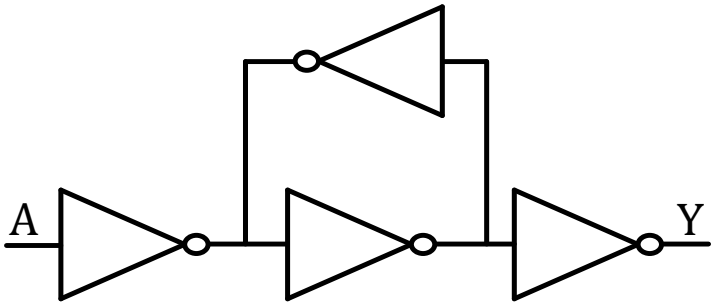

(a)

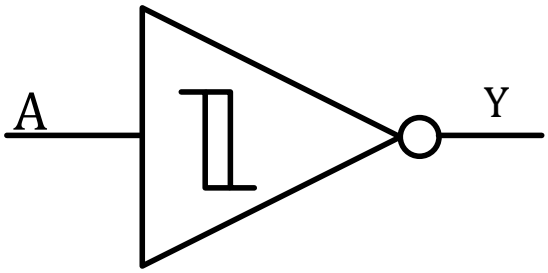

(b)

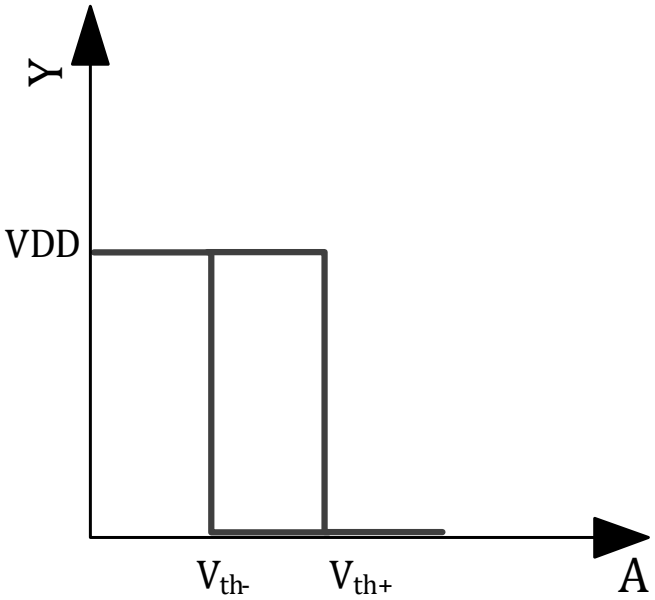

(c)

Figure 3.8 (a) Schmitt trigger inverter (b) Schmitt trigger symbol (c) Schmitt trigger VTC

The Schmitt trigger inverter can be used to build a ROSC as it uses the same operating mechanism as the analog version minus the resistor network. The oscillation frequency of this circuit is derived below.

Consider the voltage drop across the Schmitt trigger to be VDD, the voltage profile of the capacitor while charging is given by:

$$V(t) = V_i - V_{DD}\left(1 - e^{-\frac{t}{RC}}\right) + V_{DD} \tag{3.16}$$

As the capacitor is discharged to ground,

$$V(t) = V_c e^{-\frac{t}{RC}} \tag{3.17}$$

Where,

- V_i is the initial voltage across the capacitor at t = 0
- V_c is the voltage of the capacitor at the start of discharge

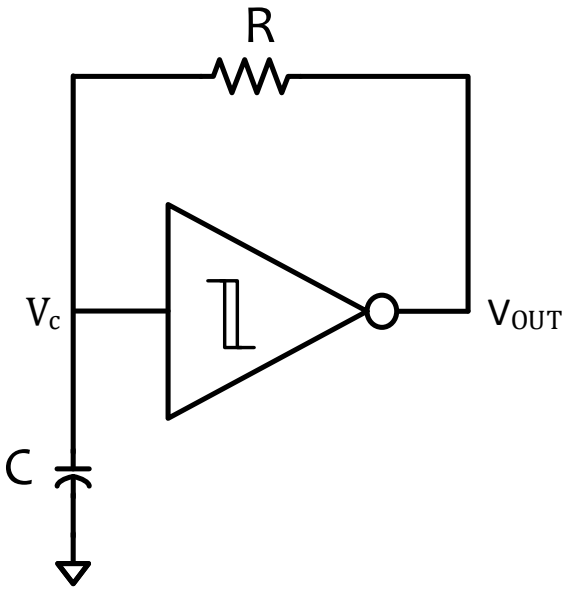

Figure 3.9 Relaxation oscillator using Schmitt trigger inverter

Now consider the ROSC circuit in Figure 3.9. The voltage drop across the capacitor varies due to the charging and discharging nature of the capacitor. Also, note that the capacitor does not fully charge to VDD or discharge to ground. This is due to the resistive feedback. Thus, the capacitor charges to the $V_{th+}$and discharges to V_{th-}. Therefore, while the capacitor is charging,

$$V_{th+} = (V_{th-} - V_{DD})\left(1 - e^{-\frac{t_c}{RC}}\right) + V_{DD} \tag{3.18}$$

Where, t_c is the time taken by the capacitor to charge

Therefore, t_c is given by

$$t_c = RC \ln\left[\frac{V_{DD} - V_{th+}}{V_{DD} - V_{th-}}\right] \tag{3.19}$$

And the time taken for the capacitor to discharge from V_{th+} to V_{th-} is given by t_d:

$$V_{th-} = V_{th+} e^{-\frac{t_d}{RC}} \tag{3.20}$$

$$t_d = RC \ln\left[\frac{V_{th+}}{V_{th-}}\right] \tag{3.21}$$

Therefore, the oscillation period of the oscillator is given by the sum of the charging discharging times of the capacitor, as referred to Figure 3.10.

$$t_{OSC} = t_d + t_c = RC \cdot \ln\left(\frac{(V_{DD} - V_{th-})V_{th+}}{(V_{DD} - V_{th+})V_{th-}}\right) \tag{3.22}$$

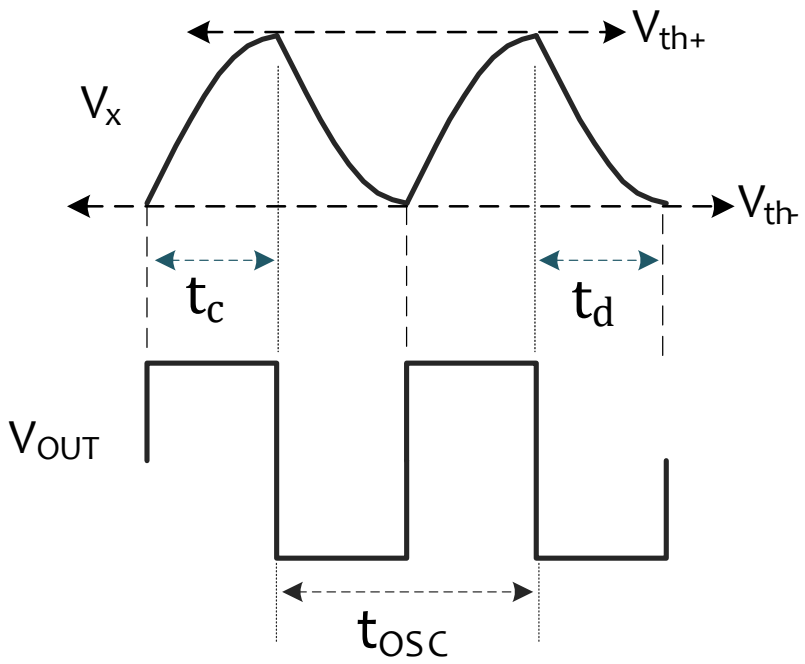

Figure 3.10 Relaxation oscillator output

From equation 3.22, we can observe that the oscillation period is directly correlated to the resistor and capacitor values, where the supply and switching threshold values are constant. By constraining the resistor to a constant value, the relationship between the capacitance and the oscillation results in a linear curve. Thus, resulting in a varying oscillation period with varying capacitance value.

The Schmitt trigger inverter ROSC is poised to be more advantageous over its analog counterpart. Firstly, the digital ROSC requires fewer components to build than the analog version as the resistive network is not required. Secondly, the Schmitt trigger gate required one supply voltage, whereas the analog version has an op-amp that traditionally requires two common-mode voltages. Thirdly, the digital Schmitt trigger consumes significantly less power compared to the analog Schmitt trigger. Taken together, the relaxation oscillator designed for the sensor mote consists of the digital Schmitt trigger

inverter, with an RC network. The RC network of the sensor mote comprises the printed CSG with the resistor calibrated to operate in a nominal frequency range.

The oscillation period of the sensor mote is modified minutely to consider any parasitics accompanying the interconnect. The new oscillation period is given by equation 3.23

$$t_{OSC} = R(C_S + C_P) \cdot ln\left(\frac{(V_{DD} - V_{th-})V_{th+}}{(V_{DD} - V_{th+})V_{th-}}\right) \tag{3.23}$$

where,

- C_S is the capacitance of CSG
- C_P is the parasitic capacitance of from the interconnect
- V_{DD} is the supply voltage of the Schmitt trigger
- V_{th-} and V_{th+} are the switching thresholds of the Schmitt trigger

Thus, setting the oscillation frequency as:

$$f_{OSC} = \frac{1}{t_{OSC}} \tag{3.24}$$

Hence, in the place of the input capacitor, the printed CSG is used illustrated in Figure 3.11a. Once the static parasitic capacitance from the interconnect is compensated for, the oscillation period t_{OSC} will be perfectly linear with respect to capacitance C_S as seen in Figure 3.11b. Additionally, a high dynamic range is easily achieved by tuning the feedback resistor of the oscillator. The supply voltage, V_{DD} is precisely set by the power regulation on the wireless hub and any variability is suppressed by the decoupling capacitor on the sensor mote. The digital output of the oscillator comes with a few advantages. Firstly, any potential interference is reduced, whereas an analog output signaling would be sensitive to interference since the unshielded output wire would be routed on a 2m long

Kevlar strap. Secondly, a digital output eliminates the need for an analog-to-digital converter (ADC) on the wireless hub, as implemented in [9, 11-15], simplifying the parallelization of data readout from multiple sensor motes.

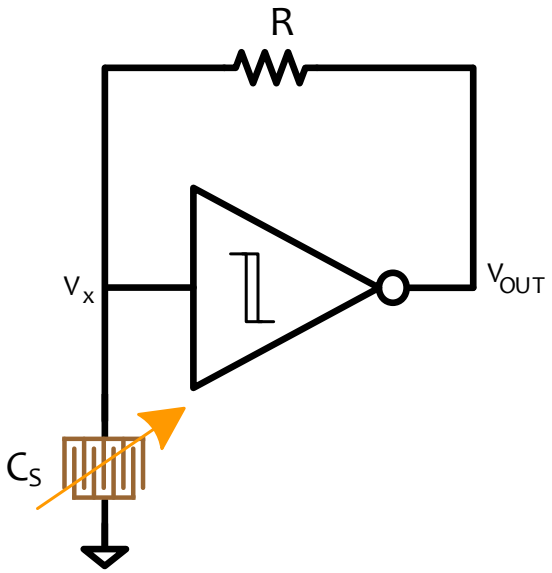

(a)

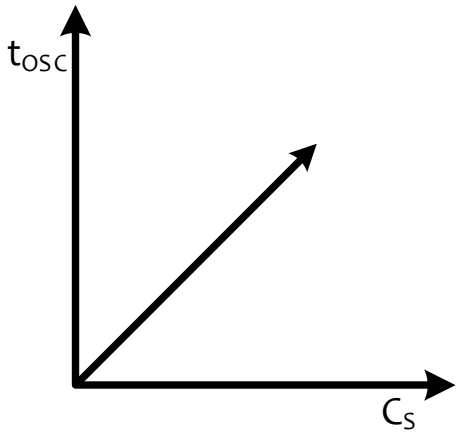

(b)

Figure 3.11 (a) Sensor mote circuit (b) Oscillation period vs CSG capacitance

Wireless Hub

Bluetooth (BT) communication provides a sense of security for the SHM system as they are intended for communication between fixed devices. BT is a short-range wireless technology standard that uses ultra-high frequency (300MHz-3GHz) radio waves in the ISM (industrial, scientific, and medical) band for data transmission [26]. The operating range of BT is between 2.402 and 2.480 GHz that accommodates 79 channels with 1MHz bandwidth per channel. It divides the data into packets and transmits the data on one of the 79 channels [26]. There are several ways to establish BT communication. Few ways to establish BT communication are listed and explained below.

- Arduino board with HC-05
- Arduino Nano 33 BLE
- Adafruit ItsyBitsy nRF52840 Express
- Adafruit feather nRF52840 Express

Arduino with HC-05

Most common BT protocol is established using an Arduino and a HC-05 BT module [27]. Arduino board is a multi-purpose evaluation board that aids in building many creative projects. It mainstreams an Atmel microcontroller such as ATmega328 with a built-in power regulation to outsource power supplies. Arduino gained popularity due to its easy-to-use hardware and software combo. Figure 3.12 illustrates the BT set-up using HC-05 and Arduino nano.

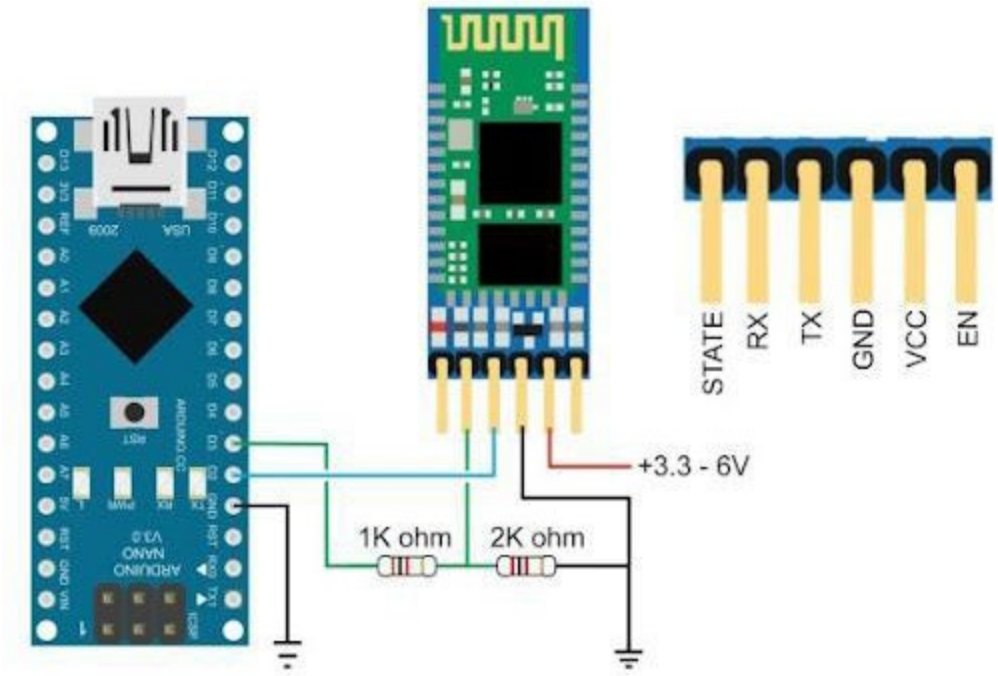

Figure 3.12 Arduino nano – HC-05 BT set-up [27]

Features of Arduino nano are summarized in Table 3.2.

Table 3.2 Features of Arduino Nano [28]

Microcontroller	ATmega328
Operating Voltage	5 V
Flash Memory	32 KB
Clock Speed	16MHz
Digital I/O pins	22
Analog IN pins	8
DC current per I/O Pin	40mA
Power consumption	19mA
PCB size	18x45mm

The HC-05 is a popular BT module that enables two-way communication. It is the most common module that is paired with an Arduino for wireless communication. It typically operates at 5V with a current consumption of 30mA. The communication between

the BT module and the microcontroller is established using universal asynchronous receiver transmitter (UART) connection [29]. It comes with a built-in Bluetooth V2.0 transceiver. The data transfer uses frequency-hopping spread spectrum that can be easily interfaced with a base station such as a laptop or mobile phones.

Though the combination of an Arduino with HC-05 is widespread, the BT communication range of the HC-05 is very limited. The coverage range of Bluetooth V2.0 is 10m which would be insufficient to be used for the SHM system of the inflatable structure, e.g., B-330 that is 330 cubic meter in volume [32]. Therefore, nRF52840 microcontroller poses as an excellent candidate.

The nRF52840 shown in Picture 3 is a BT enabled system on chip (SoC) from Nordic semiconductor that supports Bluetooth low energy (BLE). BLE radio is designed for low power consumption that is capable of transmitting data over 40 channels in 2.4GHz [30]. Each channel of BLE has 2MHz bandwidth thus lowering the power consumption. Also, nRF52840 employs a BT 5.2 radio that has a range of 400m or greater than 1300ft, making it adequate to be used for the SHM system. The features of nRF52840 are listed in Table 3.3 [31].

Picture 3. nRF52840 BLE SoC

Table 3.3 Main features of nRF52840

Frequency band	2.4GHz
Data rate	2MBs, 1Mbs, 500kbs, 125kbs
Radio power consumption	14.6mA at 8dBm output power
Microcontroller	ARM cortex-M4F
Flash memory	1MB
System power consumption	400nA

Commercially, there are several boards that accommodate the nRF52840 BLE SoC. For the design of the SHM system the Arduino 33 BLE, Adafruit ItsyBitsy nRF52840 Express, and Adafruit feather nRF52840 Express were considered.

Arduino nano 33 BLE:

The Arduino nano 33 BLE (Picture 4.) is a BT enabled board that harbors a nRF52840 SoC operating at 3.3 V. The key features of this board are listed in Table 3.4.

Picture 4. Arduino nano 33 BLE

Table 3.4 Features of Arduino nano 33 BLE

Microcontroller	nRF52840
Operating Voltage	3.3V
Flash Memory	1MB
Clock Speed	64MHz
Digital I/O pins	14
Analog IN pins	8
DC current per I/O Pin	15mA
Power consumption	15mA
PCB size	10x45mm

This board featuring the nRF52840 can operate in ultra-low power consumption modes. It makes an ideal candidate to implement high-level robotic projects, wearable devices such as exercise trackers and many more [33].

Adafruit ItsyBitsy nRF52840 Express:

Adafruit industries feature several BT enable boards. One among them is the ItsyBitsy nRF52840 Express. It employs nRF52840 like Arduino nano 33 BLE board. The key features of this board are listed in Table 3.5 [34].

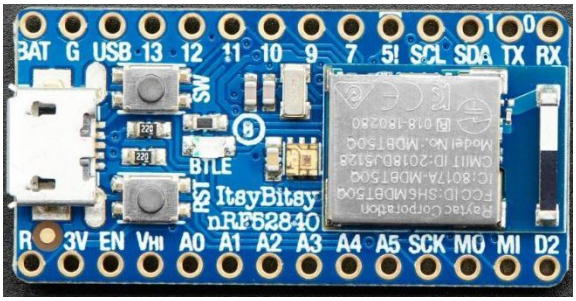

Picture 5. Adafruit ItsyBitsy nRF52840 Express

Table 3.5 Features of Adafruit ItsyBitsy nRF52840 Express

Microcontroller	nRF52840
Operating Voltage	3.3V
Flash Memory	2MB
Clock Speed	64MHz
Digital I/O pins	12
Analog IN pins	6
DC current per I/O Pin	4.8mA - 14.8mA
Power consumption	up to +8dBm
PCB size	17.6x36mm

Adding to the features summarized above in Table 3.5, the board has one special output pin that aids the high-level voltage operation, i.e., at 5V. This is processed through a digital 5 level-shifter. Also, this board can be programmed using the Arduino IDE or by python using CircuitPython through a USB serial console [34].

Adafruit Feather nRF52840 Express

This board, as seen in Picture 6, is similar to its Adafruit and Arduino counterparts. Enabling BLE, this board can be programmed to operate in low-power mode significantly reducing the overall current consumption. Although this board does not have the special high-level output pin it comes with a JST connector for battery connection, thus eliminating the need for additional circuitry for battery enabled projects. The key features of this board are listed in Table 3.6 [35].

Picture 6. Adafruit Feather nRF52840 Express

Table 3.6 Features of Adafruit Feather nRF52840 Express

Microcontroller	nRF52840
Operating Voltage	1.7V to 3.3V
Flash Memory	1MB
Clock Speed	64MHz
Digital I/O pins	12
Analog IN pins	6
DC current per I/O Pin	4.8mA - 14.8mA
Power consumption	up to +8dBm
PCB size	23x51mm

Hence, considering the features of the above-mentioned microcontroller board, Adafruit Feather nRF52840 Express was chosen as the wireless hub as it has an additional advantage of the battery connection [35]. Accommodating a Bluetooth 5.0 transceiver, this board has a coverage range of 400m making it suitable for implementation of multiple channels for distributed strain sensing of a large inflatable space structure.

Implementation of SHM system

The implementation of the proposed SHM system is illustrated in Figure 3.13. As observed the outputs of the sensor motes that are comprised of the ROSC and the printed CSG are connected to the wireless hub. The system is powered by a 250mAh, 3.7V lithium polymer battery. Rapid data acquisition is essential as the safety of the crewmembers and

the structural integrity of the structure is concerned. Also, it facilitates any quick fixes if needed. Therefore, the system is sampled at 100Hz or 10ms. This implies that the frequency count of the sensor mote is read by the SoC every 10ms. Thus, considering the 100Hz sampling rate and the clock speed of Bluetooth SoC that is 64MHz, the system provides over 75dB of dynamic range with time reserved for oversampling. This alleviates the lack of an oscillator-microcontroller synchronization and wireless data transmission, i.e., additional elements such as an ADC.

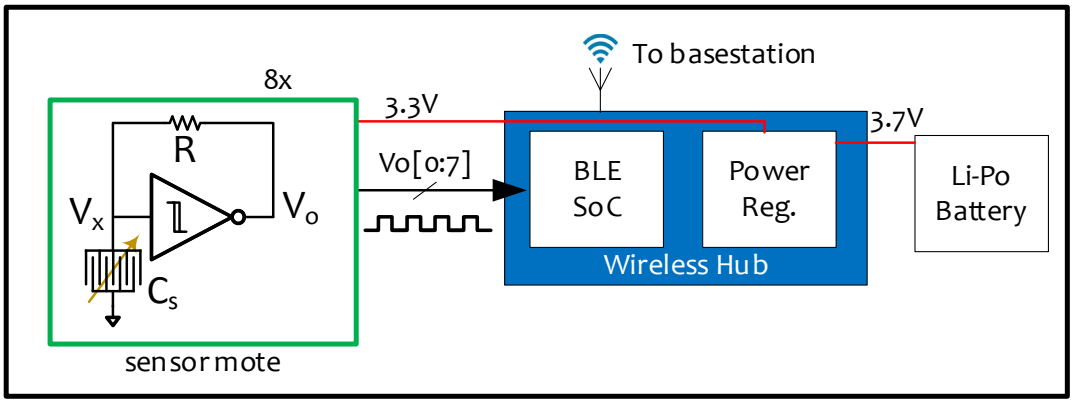

Figure 3.13 Illustration of the SHM System

Picture 7b shows the test fixture of the SHM system. The components used are summarized in Table 3.7. The sensor mote has a decoupling capacitor that suppresses any variability from the power supply as seen in Picture 7a. Verification of the system details that the Schmitt trigger consumes about 1mA at 3.3V and the wireless hub consumes 7.6mA giving a battery life of 15 hours. The selected feedback resistors set a nominal frequency range of 10kHz to 40kHz to accommodate the capacitance range well beyond the intrinsic range of the CSG.

Table 3.7 System Components

Schmitt trigger	TI SN74AUP1G14
Feedback resistor	5MΩ
Decoupling capacitor	0.01µF
Wireless hub	Adafruit Feather nRF52840 Express

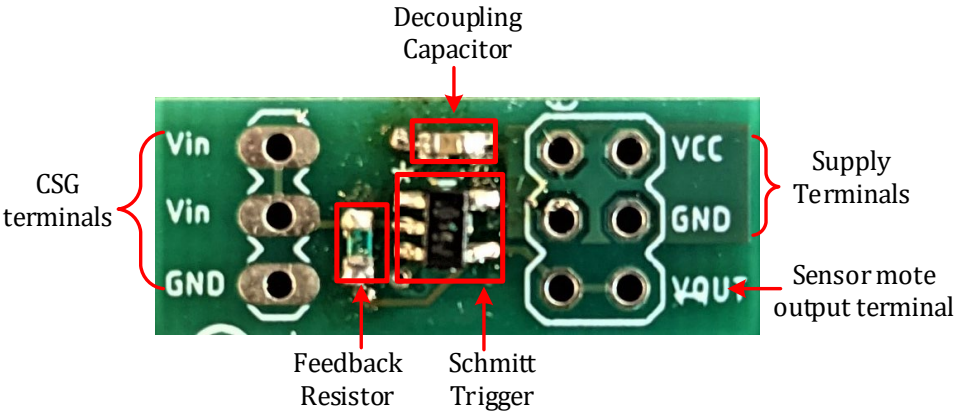

(a)

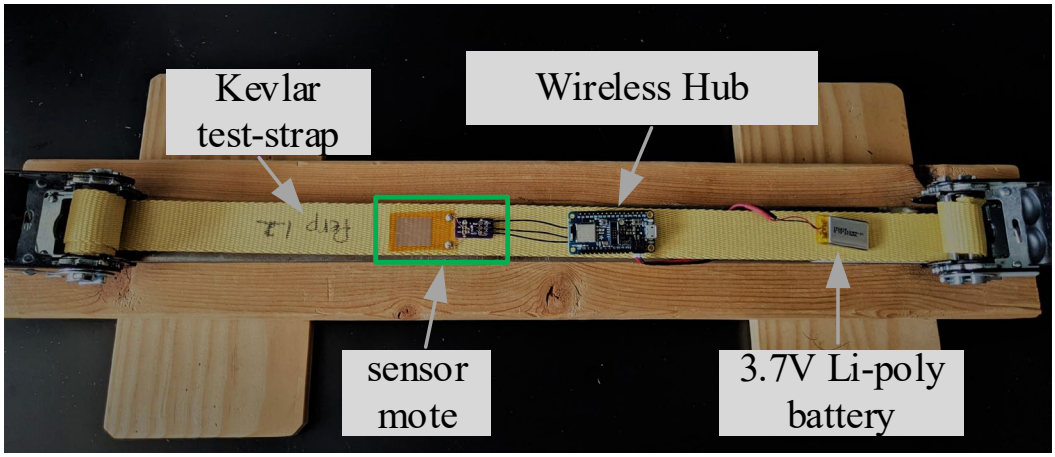

(b)

Picture 7. (a) Sensor Mote Interconnect (b) Test Fixture of the System

CHAPTER FOUR: RESULTS AND CONCLUSION

In this chapter, validation and verification of the system is discussed that are categorized by:

- Oscillator performance
- Real-time strain measurement
- Multi-channel data acquisition

Oscillator Performance

The oscillator performance is characterized by its linearity of the oscillation period with respect to varying capacitance and its sensitivity which is measured through period jitter.

Oscillator Linearity

Validating for the linear response of the oscillation period with respect to capacitance of the sensor mote, discrete capacitive loads were used. The capacitor values ranged from 5 pF to 45nF, which accommodates the intrinsic printed CSG capacitance range (42pF to 15nF). To determine the capacitance value, the switching thresholds were measured, where V_{th-} and V_{th+} were 0.97V and 1.56V respectively for V_{DD}= 3.3V. Thus, substituting these values in equation 3.23, with feedback resistor value of 5MΩ we get the oscillation period $t_{OSC} = 0.81 \cdot R(C_S + C_P)$.

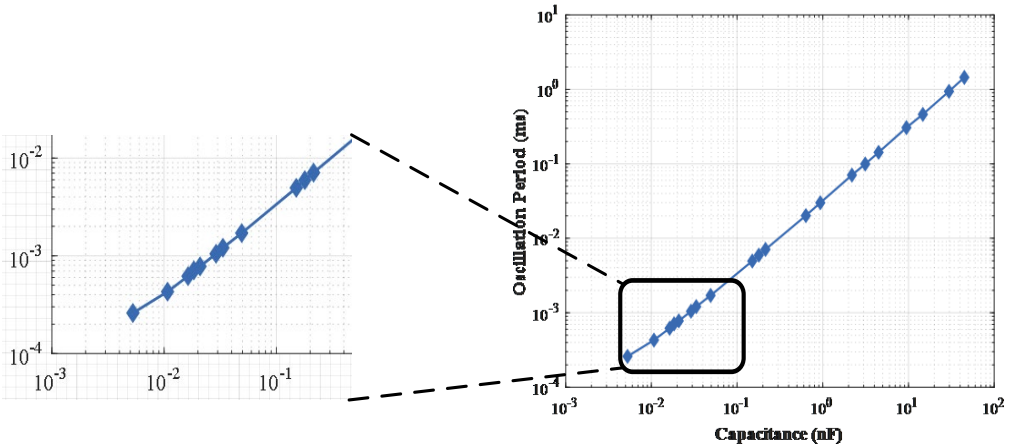

Figure 4.1 Initial Oscillator Performance

The initial results of this testing can be seen in Figure 4.1. In this plot, we can see that there is some initial non-linearity. This is due to the static parasitic capacitance from the interconnect, that was discussed in equation 3.23, which measures to 5pF. After correcting for the parasitic capacitance, the relationship between oscillation period and capacitance is highly linear as seen in Figure 4.2.

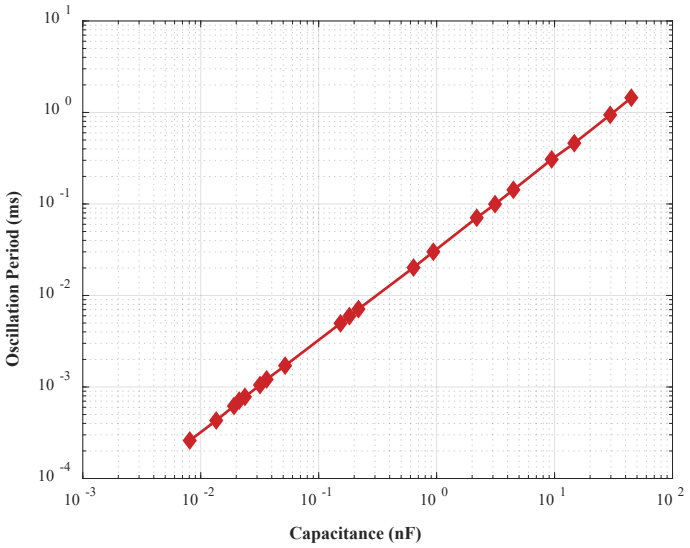

Figure 4.2 Oscillation Period versus Capacitance after Compensation [$R^2 = 0.9999$]

Oscillator Sensitivity:

The sensitivity of the oscillator sets the capacitance resolution. Since the output of the sensor mote is a digital clock signal, this sensitivity is determined by jitter. Jitter determines the sensitivity of a synchronous circuitry or circuit that outputs digital clocks. It is the difference between one clock period to the ideal or average clock period [36]. Often, jitter is also referred to the uncertainty caused by the variation in the position of the alternating edge of a digital signal, as seen in Figure 4.3. The jitter equation is given by:

$$\Delta t = 0.81 \cdot (R \cdot \Delta C) \tag{4.1}$$

Therefore, the jitter measured for the oscillator was 143.8ns for 15kHz oscillation, this sets the capacitance resolution of 35fF by substituting the feedback resistor value of 5MΩ, making it highly sensitive to subtle changes in strain via capacitance.

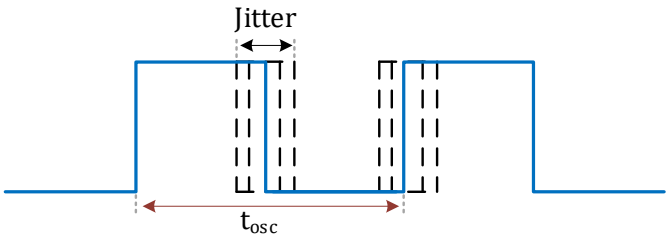

Figure 4.3 Pictorial Representation of Jitter

Although the oscillator shows high linearity and sensitivity, the overall system performance is limited by the wireless hub. With the microcontroller's clock rate of 64MHz, high frequency measurement, i.e., small capacitance that is in the order of fF cannot be measured. The system performance is also sampling rate limited, i.e., large capacitance that is greater than 100nF cannot be accounted for. Figure 4.4 figuratively illustrates the oscillator limitations.

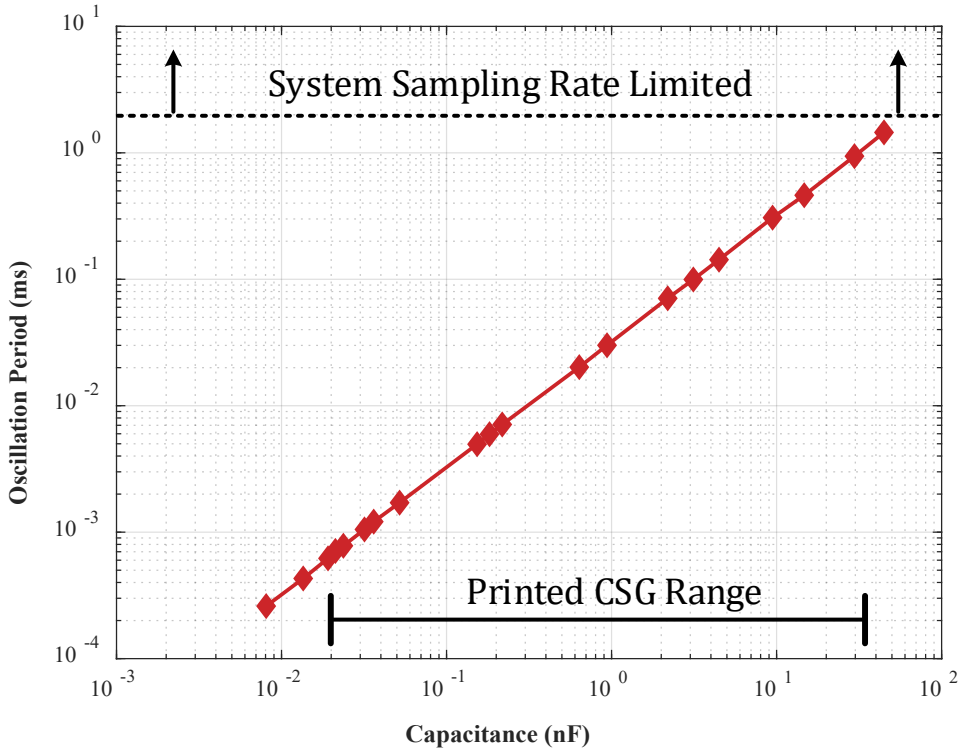

Figure 4.4 Nominal Oscillator Performance

Real-time Stain Measurement

To verify the integrity of the readout system in real time, a single printed CSG was used for strain measurement under controlled conditions. The experimental set-up comprised of a material test system and a sensor mote, as seen in picture 8. For the sensor mote, the CSG used was printed on a layer of ceramic cement on a flat plate ASTM tensile specimen i.e., an aluminum alloy (Al-6061) tensile specimen that encompasses the shape of a dog bone as illustrated in Picture 8a. The ends of this tensile specimen are attached to the hydraulic grip of the MTS as seen in Picture 8b. The bottom of the hydraulic grip is connected to an actuator that pulls the ends of the aluminum dog bone. For data acquisition, the printed CSG was connected to the relaxation oscillator by a 725mm long three conductor twisted cable that has an inherent capacitance of 52pF.

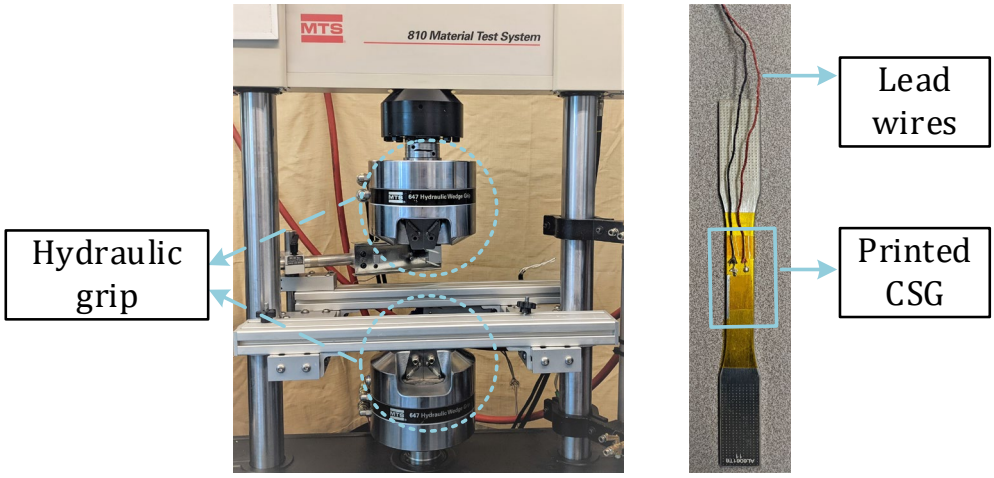

(a)

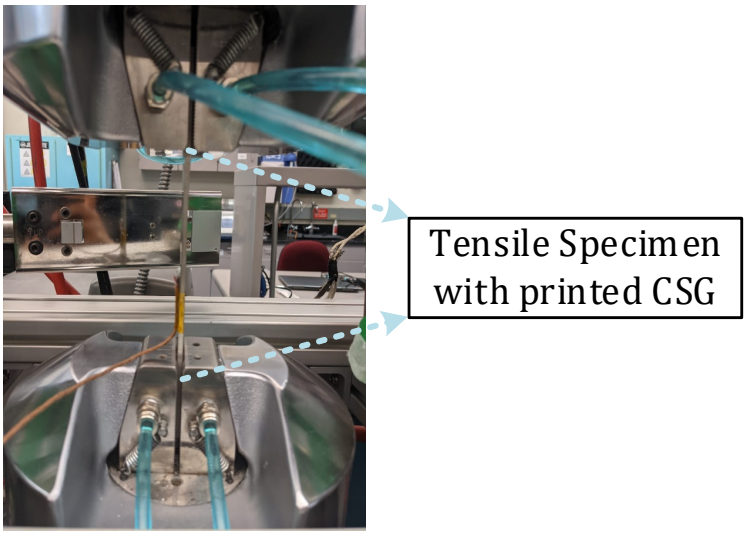

(b)

Picture 8 (a) MTS and ATSM Tensile Specimen (b) Measurement set-up

Referring to equations 2.6 – 2.8, the capacitance of the printed CSG should decrease with increasing strain. Therefore, as the dog bone was incrementally strained, the distance between the interdigitated electrodes increases, thus decreasing the CSG capacitance. Figure 4.5 shows the measured capacitance change due to applied strain and the correlation between the designed readout system and LCR meter.

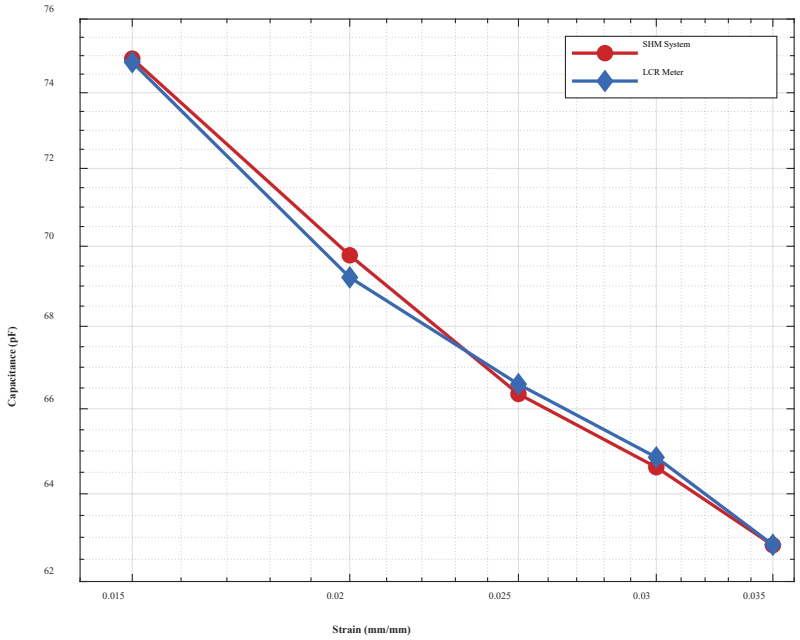

Figure 4.5 Measured capacitance change due to applied strain

Multi-channel data acquisition

For the multi-channel data acquisition, the measurement set-up consisted of a function generator and the wireless hub. The function generator used was Analog discovery 2 developed by Analog devices is a universal serial bus (USB) enabled multi-instrument equipment that employs an oscilloscope, logic analyzer, and multi-function instruments allowing users to measure, visualize, generate, record, and control mixed-signal circuits [37]. Therefore, for wireless, multi-channel data acquisition of the proposed SHM system validation, the eight sensor motes were emulated by using eight independent clock signals from the Analog Discovery 2 function generator. For the function generator to output different clock frequencies impersonating the sensor motes, look-up tables of the clock frequencies were pre-generated using MATLAB. Figure 4.6 shows the frequency waveforms.

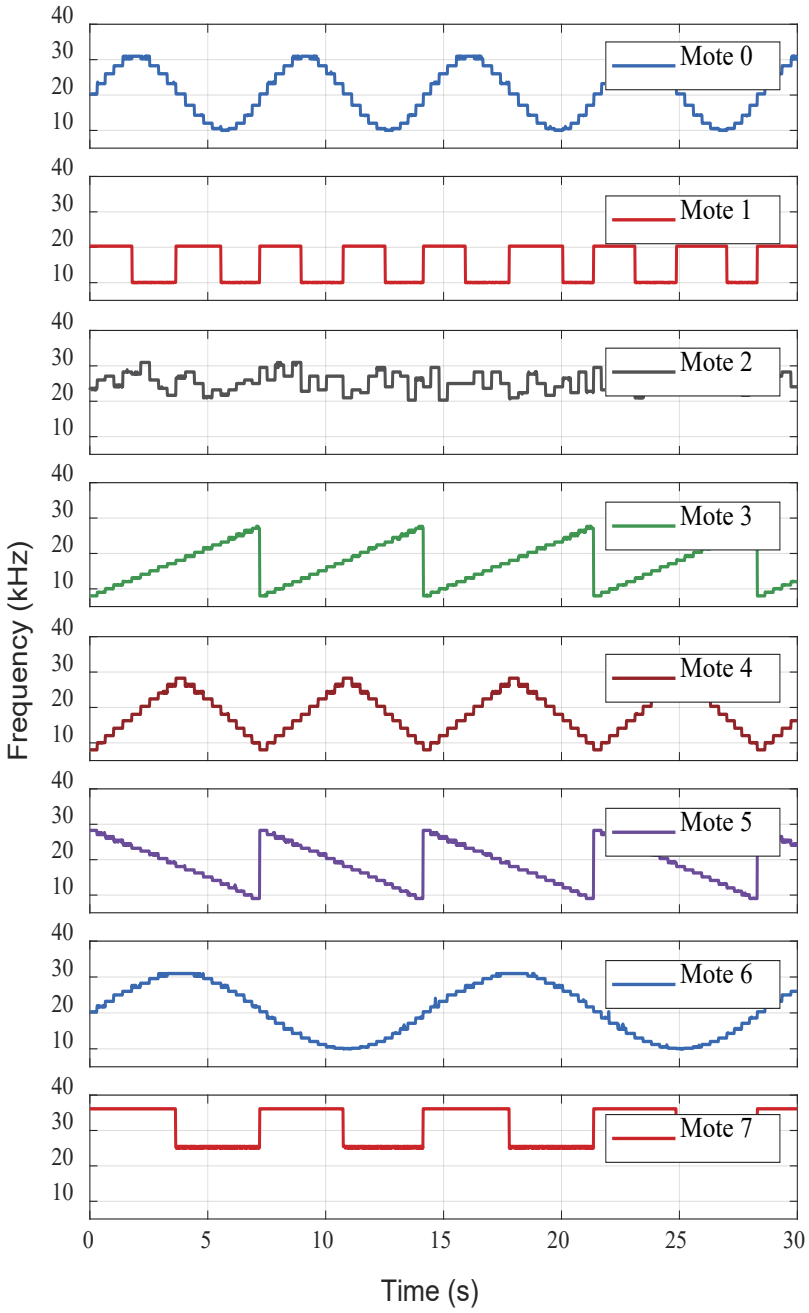

Figure 4.6 Real-time, multi-channel acquisition of independent, frequency varying signals

The generated look-up table data was then fed into the function generator's firmware such that the function generator could update the output frequency every 300ms. Considering that the output of the mote is a square wave signal whose frequency changes

over time, the output from the function generator follows various patterns such as sinusoidal, square wave, sawtooth, and gaussian noise to mimic different rates of applied strain. The output of the measure output frequencies sampling at 100Hz for all eight channels can be seen in Figure 4.6, which showed good agreement with the pre-generated frequency profiles that updated every 300ms.

Conclusion

Softgoods are high tensile fabrics that are lightweight and flexible making them advantageous to be used in construction of inflatable structures in the space industry. But accounting for the structural integrity has been a challenging mission for engineers. Conventional structural health monitoring systems cannot be used for these inflatable structures. As they take on their final form through pressurized air, strain monitoring is essential. Therefore, printed capacitive strain gauges are a promising technology for structural monitoring of soft structural materials; however, there is a lack of a practical readout system for them. To meet this need, a structural health monitoring system is presented for distributed and wireless monitoring with flexible capacitive strain gauges. The system demonstrates excellent linearity and dynamic range using a capacitance-to-frequency readout. The presented system is optimized for use with a Kevlar strap common to space habitat construction and can be scaled to a higher channel count by using additional hubs on other straps. This system could help ensure the integrity of a space habitat and safety of the crewmembers.

REFERENCES

[1] K. T. Fujimoto, J. K. Watkins, T. Phero, D. Litteken, K. Tsai, T. Bingham, K. L. Ranganatha, B. C. Johnson, Z. Deng, B. Jaques, and D. Estrada, "Aerosol jet printed capacitive strain gauge for soft structural materials," npj Flexible Electronics, vol. 4, no. 1, 2020.

[2] D. Litteken, "Evaluation of Strain Measurement Devices for Inflatable Structures," 58th AIAA/ASCE/AHS/ASC Structures, Structural Dynamics, and Materials Conference, 2017.

[3] S.-R. Kim, J.-H. Kim, and J.-W. Park, "Wearable and Transparent Capacitive Strain Sensor with High Sensitivity Based on Patterned Ag Nanowire Networks," ACS Applied Materials $\&$ Interfaces, vol. 9, no. 31, pp. 26407–26416, 2017.

[4] D. J. Cohen, D. Mitra, K. Peterson, and M. M. Maharbiz, "A Highly Elastic, Capacitive Strain Gauge Based on Percolating Nanotube Networks," Nano Letters, vol. 12, no. 4, pp. 1821–1825, 2012.

[5] F.-X. Wang, J. Lin, W.-B. Gu, Y.-Q. Liu, H.-D. Wu, and G.-B. Pan, "Aerosol-jet printing of nanowire networks of zinc octaethylporphyrin and its application in flexible photodetectors," Chemical Communications, vol. 49, no. 24, p. 2433, 2013.

[6] J. A. Paulsen, M. Renn, K. Christenson, and R. Plourde, "Printing conformal electronics on 3D structures with Aerosol Jet technology," 2012 Future of Instrumentation International Workshop (FIIW) Proceedings, 2012.

[7] R. Zeiser, T. Fellner, and J. Wilde, "Capacitive strain gauges on flexible polymer substrates for wireless, intelligent systems," Journal of Sensors and Sensor Systems, vol. 3, no. 1, pp. 77–86, 2014.

[8] J. Hinkle, G. Sharpe, J. Lin, C. Wiley, and R. Timmers. “Intelligent Flexible Materials for Space Structures,” NASA Scientific and Technical Information Program. Technical Report No. NASA/CR–2010-216682, 2010.

[9] Admin, “Stress and strain - definition, stress-strain curve, Hooke's law, Si Units,” BYJUS, 30-Sep-2021. [Online]. Available: https://byjus.com/physics/stress-and-strain/#what-is-strain. [Accessed: 10-Oct-2021].

[10] Omega Engineering. [Online]. Available: https://www.omega.co.uk/prodinfo/StrainGauges.html. [Accessed: 10-Oct-2021].

[11] B. McGinty, Strain gauges. [Online]. Available: https://www.continuummechanics.org/straingauges.html. [Accessed: 10-Oct-2021].

[12] “Strain gauge,” Encyclopædia Britannica. [Online]. Available: https://www.britannica.com/technology/strain-gauge. [Accessed: 10-Oct-2021].

[13] “Piezoresistive pressure sensors,” Avnet. [Online]. Available: https://www.avnet.com/wps/portal/abacus/solutions/technologies/sensors/pressure-sensors/core-technologies/piezoresistive-strain-gauge/. [Accessed: 10-Oct-2021].

[14] H. Gullapalli, V. S. Vemuru, A. Kumar, A. Botello-Mendez, R. Vajtai, M. Terrones, S. Nagarajaiah, and P. M. Ajayan, “Flexible piezoelectric zno-paper nanocomposite strain sensor,” Small, vol. 6, no. 15, pp. 1641–1646, 2010.

[15] “Comparing strain gauges to piezoelectric sensors,” Tacuna Systems, 03-Mar-2021. [Online]. Available: https://tacunasystems.com/knowledge-base/comparing-strain-gauges-to-piezoelectric-sensors/. [Accessed: 10-Oct-2021].

[16] S.-R. Kim, J.-H. Kim, and J.-W. Park, “Wearable and transparent capacitive strain sensor with high sensitivity based on patterned AG Nanowire Networks,” ACS Applied Materials & Interfaces, vol. 9, no. 31, pp. 26407–26416, 2017.

[17] S.-R. Kim, J.-H. Kim, and J.-W. Park, “Wearable and transparent capacitive strain sensor with high sensitivity based on patterned AG Nanowire Networks,” ACS Applied Materials & Interfaces, vol. 9, no. 31, pp. 26407–26416, 2017.

[18] M. Sidorov, P. V. Nhut, Y. Matsumoto, and R. Ohmura, “LoRa-Based Precision Wireless Structural Health Monitoring System for Bolted Joints in a Smart City Environment,” IEEE Access, vol. 7, pp. 179235–179251, 2019.

[19] R. Zeiser, T. Fellner, and J. Wilde, “Capacitive strain gauges on flexible polymer substrates for wireless, intelligent systems,” Journal of Sensors and Sensor Systems, vol. 3, no. 1, pp. 77–86, 2014.

[20] D. Brunelli, F. Di Nuzzo, T. Polonelli, and L. Benini, “Structural Health Monitoring system with Narrowband IoT and MEMS sensors,” 2021.

[21] R. Matsuzaki and A. Todoroki, “Wireless flexible capacitive sensor based on ultra-flexible epoxy resin for strain measurement of automobile tires,” Sensors and Actuators A: Physical, vol. 140, no. 1, pp. 32–42, 2007.

[22] M. C. Scardelletti, G. E. Ponchak, K. Harsh, J. A. Mackey, R. D. Meredith, C. A. Zorman, G. M. Beheim, F. W. Dynys, and G. W. Hunter, “Wireless capacitive pressure sensor operating up to 400°c from 0 to 100 psi utilizing power scavenging,” 2014 IEEE Topical Conference on Wireless Sensors and Sensor Networks (WiSNet), 2014.

[23] G. E. Ponchak, M. C. Scardelletti, J. L. Jordan, “30 and 90MHz oscillators operating through 450 and 470°C for high temperature wireless sensors,” *Asian Pacific Microwave Conference*, 2010, pages 1027-1030.

[24] D. A. Bell and D. A. Bell, in Operational amplifiers and Linear ICS, Third., Don Mills, Ont.: Oxford University Press, 2010, pp. 182–187.

[25] Electrical4U, “Schmitt gates (Nand Schmitt trigger gates),” Electrical4U, 28-Oct-2020. [Online]. Available: https://www.electrical4u.com/schmitt-gates/. [Accessed: 12-Oct-2021].

[26] “Bluetooth,” Wikipedia, 12-Oct-2021. [Online]. Available: https://en.wikipedia.org/wiki/Bluetooth. [Accessed: 12-Oct-2021].

[27] M. Currey, “Arduino With HC-05 Bluetooth Module in Slave Mode,” Martyn Currey, 27-Oct-2014. [Online]. Available: http://www.martyncurrey.com/arduino-with-hc-05-bluetooth-module-in-slave-mode/. [Accessed: 13-Oct-2021].

[28] “Arduino Nano,” *Arduino Online Shop*. [Online]. Available: https://store-usa.arduino.cc/products/arduino-nano?selectedStore=us. [Accessed: 14-Oct-2021].

[29] “HC-05 - Bluetooth module,” Components101. [Online]. Available: https://components101.com/wireless/hc-05-bluetooth-module. [Accessed: 14-Oct-2021].

[30] “Bluetooth technology overview,” Bluetooth® Technology Website. [Online]. Available: https://www.bluetooth.com/learn-about-bluetooth/tech-overview/. [Accessed: 14-Oct-2021].

[31] “NRF52840,” Nordic Semiconductor. [Online]. Available: https://www.nordicsemi.com/Products/nRF52840. [Accessed: 14-Oct-2021].

[32] “B330,” Wikipedia, 02-Aug-2021. [Online]. Available: https://en.wikipedia.org/wiki/B330. [Accessed: 04-Oct-2021].

[33] “Arduino Nano 33 ble,” Arduino Online Shop. [Online]. Available: https://store-usa.arduino.cc/products/arduino-nano-33-ble?selectedStore=us. [Accessed: 14-Oct-2021].

[34] A. Industries, “Adafruit Itsybitsy NRF52840 Express - Bluetooth Le,” adafruit industries blog RSS. [Online]. Available: https://www.adafruit.com/product/4481. [Accessed: 14-Oct-2021].

[35] A. Industries, “Adafruit Feather NRF52840 Express,” adafruit industries blog RSS. [Online]. Available: https://www.adafruit.com/product/4062. [Accessed: 14-Oct-2021].

[36] “Jitter,” Wikipedia, 30-Jun-2021. [Online]. Available: https://en.wikipedia.org/wiki/Jitter. [Accessed: 20-Sep-2021].

[37] J. Arthur and J. Kretzschmar, “Analog Discovery 2: 100MS/s USB oscilloscope, Logic Analyzer and variable power supply,” Digilent. [Online]. Available: https://digilent.com/shop/analog-discovery-2-100ms-s-usb-oscilloscope-logic-analyzer-and-variable-power-supply/. [Accessed: 14-Oct-2021].

APPENDIX A

Wireless Hub Code

```
#include <Arduino.h>

const uint8_t mote0 = 5;

const uint8_t mote1 = 6;

const uint8_t mote2 = 9;

const uint8_t mote3 = 10;

const uint8_t mote4 = 11;

const uint8_t mote5 = 12;

const uint8_t mote6 = 13;

const uint8_t mote7 = A0;

const uint32_t oneSecond = 1000;

const uint32_t c = 5; // counts 5 pulses

uint32_t timer = 0;

uint32_t timeout = 500;

uint32_t high_time;

uint32_t low_time;

int wait = 10; //microsecond delay between measuring pulseIn

uint32_t start0 = 0;

uint32_t end0 = 0;


void setup() {

 Serial.begin(115200);

 //channel_0
```

```
pinMode(mote0,INPUT);
//digitalWrite(mote0,HIGH);
//channel_1
pinMode( mote1, INPUT);
//digitalWrite( mote1,HIGH);
//channel_2
pinMode(mote2, INPUT);
//digitalWrite(mote2,HIGH);
//channel_3
pinMode(mote3, INPUT);
//digitalWrite(mote3,HIGH);
 //channel_4
pinMode(mote4, INPUT);
//digitalWrite(mote4,HIGH);
 //channel_5
pinMode(mote5, INPUT);
// digitalWrite(mote5,HIGH);
 //channel_6
pinMode(mote6, INPUT);
// digitalWrite(mote6,HIGH);
 //channel_7
pinMode(mote7, INPUT);
//digitalWrite(mote7,HIGH);
```

```
}
void loop() {
 //channel_0
 //start0 = micros(); // start time stamp
 for (uint32_t i=c; i>0; i--) {
   high_time = pulseIn(mote0,HIGH,timeout);
   delayMicroseconds(wait);
   low_time = pulseIn(mote0,LOW,timeout);
   //Serial.print("Channel 0: ");
   Serial.print(1/((high_time+low_time)*769e-9));
   Serial.print("\t");
 }
//Serial.print("\t");
 //channel_1
 for (uint32_t i=c; i>0; i--) {
   high_time = pulseIn(mote1,HIGH,timeout);
   delayMicroseconds(wait);
   low_time = pulseIn(mote1,LOW,timeout);
   //Serial.print("Channel 1: ");
   Serial.print(1/((high_time+low_time)*769e-9));
   Serial.print("\t");
 }
//Serial.print("\t");
```

```
 //channel_2
 for (uint32_t i=c; i>0; i--) {
  high_time = pulseIn(mote2,HIGH,timeout);
  delayMicroseconds(wait);
  low_time = pulseIn(mote2,LOW,timeout);
 // Serial.print("Channel 2: ");
  Serial.print(1/((high_time+low_time)*769e-9));
  Serial.print("\t");
 }
//Serial.print("\t");
 //channel_3
 for (uint32_t i=c; i>0; i--) {
  high_time = pulseIn(mote3,HIGH,timeout);
  delayMicroseconds(wait);
  low_time = pulseIn(mote3,LOW,timeout);
  //Serial.print("Channel 3: ");
  Serial.print(1/((high_time+low_time)*769e-9));
  Serial.print("\t");
 }
//Serial.print("\t");
  //channel_4
 for (uint32_t i=c; i>0; i--) {
  high_time = pulseIn(mote4,HIGH,timeout);
```

```
  delayMicroseconds(wait);
  low_time = pulseIn(mote4,LOW,timeout);
  //Serial.print("Channel 4: ");
  Serial.print(1/((high_time+low_time)*769e-9));
  Serial.print("\t");
 }
//Serial.print("\t");
  //channel_5
 for (uint32_t i=c; i>0; i--) {
  high_time = pulseIn(mote5,HIGH,timeout);
  delayMicroseconds(wait);
  low_time = pulseIn(mote5,LOW,timeout);
  //Serial.print("Channel 5: ");
  Serial.print(1/((high_time+low_time)*769e-9));
  Serial.print("\t");
 }
//Serial.print("\t");
  //channel_6
 for (uint32_t i=c; i>0; i--) {
  high_time = pulseIn(mote6,HIGH,timeout);
  delayMicroseconds(wait);
  low_time = pulseIn(mote6,LOW,timeout);
  //Serial.print("Channel 6: ");
```

```
    Serial.print(1/((high_time+low_time)*769e-9));
    Serial.print("\t");
   }
  //Serial.print("\t");
    //channel_7
   for (uint32_t i=c; i>0; i--) {
    high_time = pulseIn(mote7,HIGH,timeout);
    delayMicroseconds(wait);
    low_time = pulseIn(mote7,LOW,timeout);
    //Serial.print("Channel 7: ");
    Serial.print(1/((high_time+low_time)*769e-9));
    Serial.print("\t");
   }
  Serial.println();
  }
```

Clock Frequencies to Function Generator Code

```
clear()
print("Running Script")
//Patterns.Channels.DIO0.Frequency.value = 1000;
//wait(5)
//Patterns.stop()
// Create an array, and then write an nested for loop!
//const ch_freq = "\ 1000 1500 2000 2500 3000 3500 4000 4500 5000 5500 6000 6500
7000 7500 8000 8500 9000 9500 10000";
const
ch_freq0=[15000,16545,17939,19045,19755,20000,19755,19045,17939,16545,15000,13
455,12061,10955,10245,10000,10245,10955,12061,13455,15000,16545,17939,19045,19
755,20000,19755,19045,17939,16545,15000,13455,12061,10955,10245,10000,10245,10
955,12061,13455,15000,16545,17939,19045,19755,20000,19755,19045,17939,16545,15
000,13455,12061,10955,10245,10000,10245,10955,12061,13455,15000,16545,17939,19
045,19755,20000,19755,19045,17939,16545,15000,13455,12061,10955,10245,10000,10
245,10955,12061,13455,15000,16545,17939,19045,19755,20000,19755,19045,17939,16
545,15000,13455,12061,10955,10245,10000,10245,10955,12061,13455,15000

];
ch_freq1=[20000,20000,20000,20000,20000,10000,10000,10000,10000,10000,20000,20
000,20000,20000,20000,10000,10000,10000,10000,10000,20000,20000,20000,20000,20
```

```
000,10000,10000,10000,10000,10000,20000,20000,20000,20000,20000,10000,10000,10
000,10000,10000,20000,20000,20000,20000,20000,10000,10000,10000,10000,10000,20
000,20000,20000,20000,20000,20000,10000,10000,10000,10000,20000,20000,20000,20
000,20000,10000,10000,10000,10000,10000,20000,20000,20000,20000,20000,20000,10
000,10000,10000,10000,20000,20000,20000,20000,20000,10000,10000,10000,10000,10
000,20000,20000,20000,20000,20000,20000,10000,10000,10000,10000,20000
];
ch_freq2=[20502,21225,20870,17077,18012,19709,17305,23443,16948,17259,16707,17
277,19357,18111,24234,19302,16848,24049,24797,19389,16111,17581,19087,20949,17
622,21028,22112,17217,16174,17967,18188,19242,20079,15855,17625,23010,15292,24
289,22303,19886,20785,17373,19588,24631,20468,20211,17316,19889,21241,21791,18
955,18674,24880,15377,23852,24133,22962,15987,17619,18354,21797,16366,22212,16
068,21538,19942,22791,22150,24037,23909,18342,21987,16978,15305,22441,20000,19
799,24047,21099,21177,23594,23055,20767,16829,17399,23865,15287,19899,16679,24
787,22127,20005,19711,15596,21820,15424,15714,20216,15967,23181,23175
];
ch_freq3=[3000,4000,5000,6000,7000,8000,9000,10000,11000,12000,13000,14000,1500
0,16000,17000,18000,19000,20000,21000,22000,3000,4000,5000,6000,7000,8000,9000,
10000,11000,12000,13000,14000,15000,16000,17000,18000,19000,20000,21000,22000,
3000,4000,5000,6000,7000,8000,9000,10000,11000,12000,13000,14000,15000,16000,17
000,18000,19000,20000,21000,22000,3000,4000,5000,6000,7000,8000,9000,10000,1100
0,12000,13000,14000,15000,16000,17000,18000,19000,20000,21000,22000,3000,4000,5
```

```
000,6000,7000,8000,9000,10000,11000,12000,13000,14000,15000,16000,17000,18000,1
9000,20000,21000,22000,3000
];
ch_freq4=[3000,5000,7000,9000,11000,13000,15000,17000,19000,21000,23000,21000,1
9000,17000,15000,13000,11000,9000,7000,5000,3000,5000,7000,9000,11000,13000,150
00,17000,19000,21000,23000,21000,19000,17000,15000,13000,11000,9000,7000,5000,3
000,5000,7000,9000,11000,13000,15000,17000,19000,21000,23000,21000,19000,17000,
15000,13000,11000,9000,7000,5000,3000,5000,7000,9000,11000,13000,15000,17000,19
000,21000,23000,21000,19000,17000,15000,13000,11000,9000,7000,5000,3000,5000,70
00,9000,11000,13000,15000,17000,19000,21000,23000,21000,19000,17000,15000,1300
0,11000,9000,7000,5000,3000
];
ch_freq5=[23000,22000,21000,20000,19000,18000,17000,16000,15000,14000,13000,12
000,11000,10000,9000,8000,7000,6000,5000,4000,23000,22000,21000,20000,19000,180
00,17000,16000,15000,14000,13000,12000,11000,10000,9000,8000,7000,6000,5000,400
0,23000,22000,21000,20000,19000,18000,17000,16000,15000,14000,13000,12000,1100
0,10000,9000,8000,7000,6000,5000,4000,23000,22000,21000,20000,19000,18000,17000
,16000,15000,14000,13000,12000,11000,10000,9000,8000,7000,6000,5000,4000,23000,
22000,21000,20000,19000,18000,17000,16000,15000,14000,13000,12000,11000,10000,
9000,8000,7000,6000,5000,4000,23000
];
ch_freq6=[15000,15782,16545,17270,17939,18536,19045,19455,19755,19938,20000,19
938,19755,19455,19045,18536,17939,17270,16545,15782,15000,14218,13455,12730,12
```

```
061,11464,10955,10545,10245,10062,10000,10062,10245,10545,10955,11464,12061,12
730,13455,14218,15000,15782,16545,17270,17939,18536,19045,19455,19755,19938,20
000,19938,19755,19455,19045,18536,17939,17270,16545,15782,15000,14218,13455,12
730,12061,11464,10955,10545,10245,10062,10000,10062,10245,10545,10955,11464,12
061,12730,13455,14218,15000,15782,16545,17270,17939,18536,19045,19455,19755,19
938,20000,19938,19755,19455,19045,18536,17939,17270,16545,15782,15000

];
ch_freq7=[20000,20000,20000,20000,20000,20000,20000,20000,20000,20000,10000,10
000,10000,10000,10000,10000,10000,10000,10000,20000,20000,20000,20000,20
000,20000,20000,20000,20000,20000,10000,10000,10000,10000,10000,10000,10000,10
000,10000,10000,20000,20000,20000,20000,20000,20000,20000,20000,20000,10
000,10000,10000,10000,10000,10000,10000,10000,10000,20000,20000,20000,20
000,20000,20000,20000,20000,20000,20000,10000,10000,10000,10000,10000,10000,10
000,10000,10000,10000,20000,20000,20000,20000,20000,20000,20000,20000,20
000,10000,10000,10000,10000,10000,10000,10000,10000,10000,20000
];



wait(7)
//for(var c = 0; c < 8; c++){
for(var i=0; i< 101; i++){
Patterns.Channels.DIO0.Frequency.value = ch_freq0[i];
```

```
Patterns.Channels.DIO1.Frequency.value = ch_freq1[i];

Patterns.Channels.DIO2.Frequency.value = ch_freq2[i];

Patterns.Channels.DIO3.Frequency.value = ch_freq3[i];

Patterns.Channels.DIO4.Frequency.value = ch_freq4[i];

Patterns.Channels.DIO5.Frequency.value = ch_freq5[i];

Patterns.Channels.DIO6.Frequency.value = ch_freq6[i];

Patterns.Channels.DIO7.Frequency.value = ch_freq7[i];

print(i);

Patterns1.run()

wait(.3)

}

Patterns.stop()
```

APPENDIX B

Senor Mote Interconnect

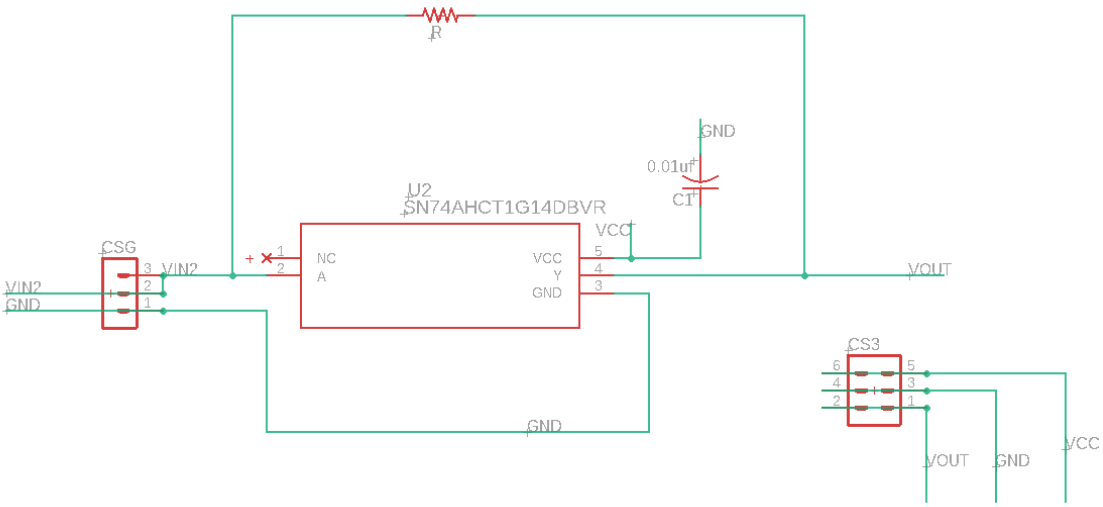

(a)

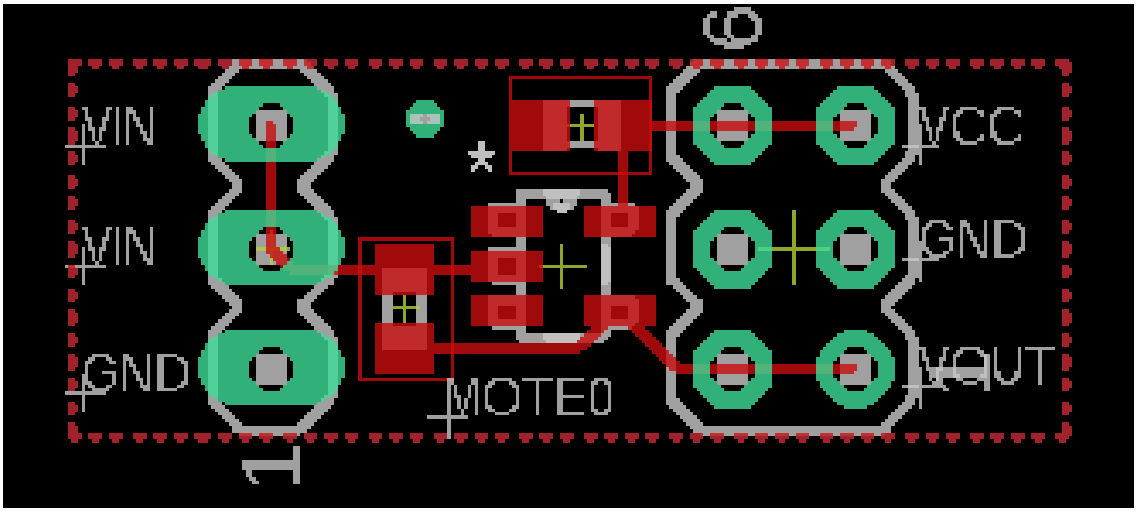

(b)

Figure B.1 Sensor Mote Interconnect :(a) Schematic (b) Layout

Driver Management Board

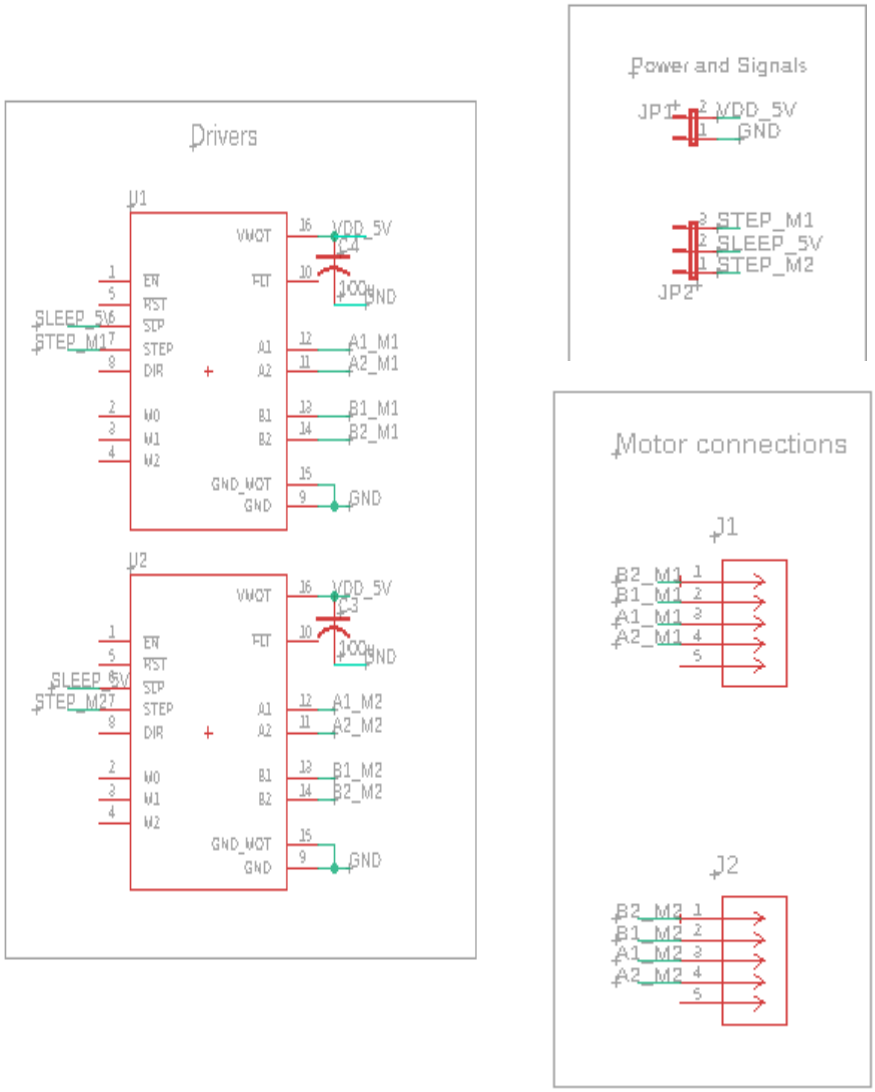

(a)

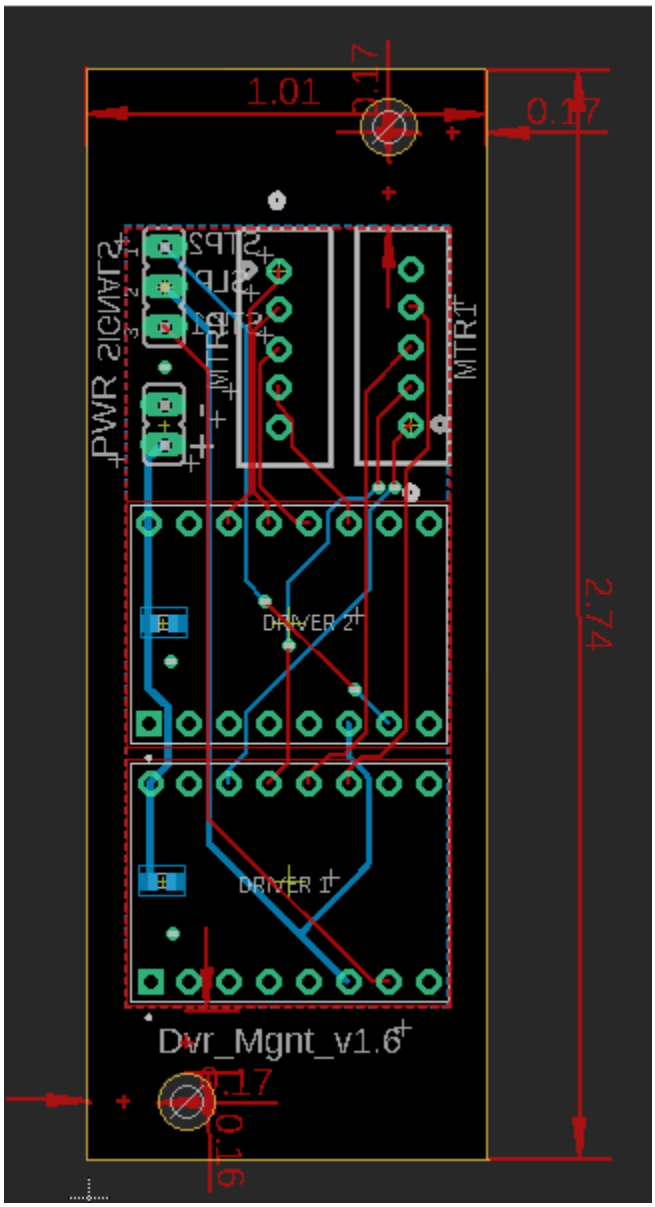

(b)

Figure B.2 Driver management Board :(a) Schematic (b) Layout

APPENDIX C

A High throughput economical Fish-feeder System

The focus of this chapter is to emphasize my work during my Master of Science degree apart from the SHM system. This chapter details the electrical system of a large-scale fish feeder system that is designed to dispense food for 50 – 65 small sized fish tanks. The software aspect of this system is beyond the scope of this thesis.

Zebrafishes are extensively used to address some essential questions that arise in basic and applied research. Even many biomedical, toxicology, and biotechnological studies employ them for their research. The high demand of these fishes is due to their proven trait for genetic screening of human diseases and carry out cellular investigations that are difficult to implement in mammalian anatomy. To facilitate these in-dept investigation in Zebrafishes, the fishes are housed in a highly sophisticated research system. With many housing solutions available, one such example of the research system is Active Blue Stand Alone, seen in Picture 9a, provided by the Aquatic solutions from Techniplast. This system consists of five rows of 10 3.5L fish tanks (Picture 9b) and 15 1.1L fish tanks (Picture 9c) totaling to 130 fish tanks .

The zebrafish research system features include:

- Mechanical drum filtration for efficient maintenance
- High UV disinfection rate
- Touch screen monitoring system with remote capabilities
- No mechanical consumables
- USB port for data logs

(a)

(b)

(c)

Picture C1 (a) Active Blue Stand Alone (b) 1.1L Fish Tank (c) 3.5L Fish Tank

In an ideal scenario, each of these fish tanks house a pair of fishes that are isolated with a plastic barrier. Monitoring their behavior would mean meticulous monitoring of their food schedule. Given the scale of the system with 65 fish tanks, would mean a tedious

feeding process. Therefore, there is a need for a high-through put feeding system that is highly reliable and cost efficient. The feeding system should also include the capability for remote and manual control, and the specificity of which tank or group of tanks are fed. The detailed specifications of the system are listed below:

- Remote control via cloud or internet
- Be able to feed groups or individual tanks
- Feed two times a day in eight- and 16-hour intervals
- Cost efficient
- Facilitate multiple forms of food (powder, pellets, and live food)

Techniplast is a full-service aquatic research equipment provider. Along with the fish housing system as seen in picture 8a, they provide an automatic feeding system known as Tritone, seen in Picture 10, that meets most of the requirements. The drawback of this feeding system is the cost as it lies in a few hundred thousand dollars.

Picture C2. Tritone: Automatic Feeding System

Thus, to reduce the spending cost for the feeding system, a new automatic feeding system, that would potentially cost a few thousand dollars with iterative testing, is designed to meet the required specifications that is remotely controllable with the use of an Arduino microcontroller board and Raspberry Pi.

System Architecture

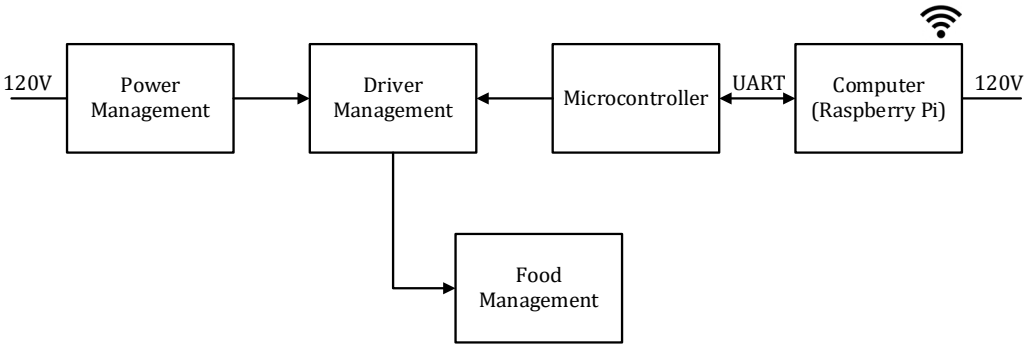

Figure C.1 Fish Feeder System Architecture

An easy to build fish feeder system is presented in [39]. Here, a 3D printed food dispenser is designed that accommodates a unipolar stepper motor, 28BYJ-48 and an ULN2003A stepper motor driver. The driver is controlled by the Arduino microcontroller board. The feeder system dispenses food for 7 days, twice a day with a 8-hour interval in the day and a 16-hour interval in the night. Inspired by this simple design, the large-scale system is designed. The system architecture is presented in Figure 5.1. Here, the power management system is connected to the 120V electrical wall-outlet which is connected to the driver management system that controls the food management system which comprises a 3D printed food dispensing bracket housing two stepper motors. The driver management is controlled by the ATMega32 microcontroller on the Arduino board which is connected to the raspberry pi for remote control. The power management uses 120V AC to 5V DC

power supply adapter to power up the entire system apart from raspberry pi. The focus of this chapter is the electrical system design detailed in driver management section.

Driver management

Picture 11 illustrates the driver management board. The system comprises of two low power stepper motor drivers, stepper motor control pins, and driver to motor connections. The stepper motor driver used is DRV8834, a low power driver board that is designed drive a bipolar motor. The job of the driver is to drive the motor by supplying the required current. The details of the driver are summarized in Table 5.1. The motor control signals are STP1, STP2 and SLP. Here, STP1 and STP2 are the step signals from the microcontroller to each driver. The step signal tells the driver to rotate the motor to for food dispensing. The sleep signal though not essential in the system is recommended to be enabled high. Once the communication between the driver and microcontroller is established, the driver drives the motor. The board has a 100uF decoupling capacitor to suppress variability from the power supplies.

Table C.1 DRV8834 driver specifications

Operating range	2.5V - 10.8V
Continuous current	1.5A
Maximum current	2A
Minimum logic voltage	2.5V
Maximum Logic Voltage	5.5V
Size	0.6in x 0.8in

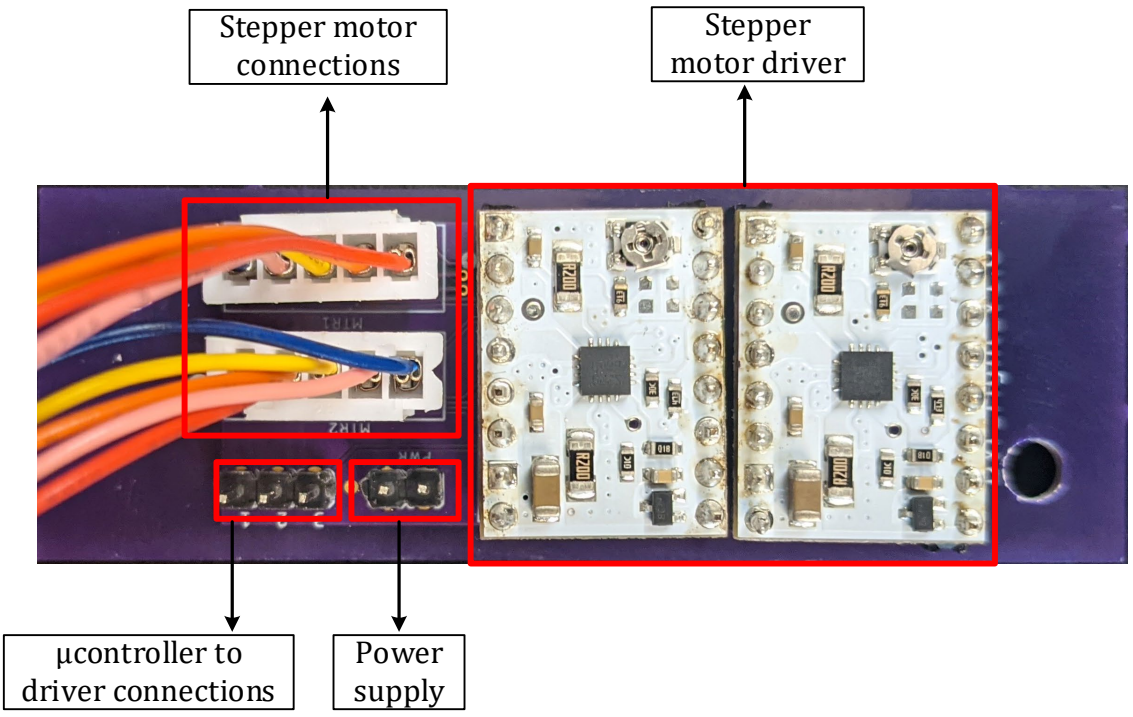

Picture C3 Driver management board

The motor used for the food management system is 28BYJ-48. This is a unipolar motor that consumes about 250mA of current. The stepper motor encompasses two sets of coil windings. The unipolarity of the motor is established by a making common connection between the two coil windings, as seen in Figure 5.2. The most common driver used to drive this motor is ULN2003A. The ULN2003A consists of 7 Darlington transistors that supplies an output current of 500mA. The drawback with this set-up is the need for four signals from the microcontroller to the driver especially considering the scale of the feeding system. Alternatively, the unipolar motor can be turned into bipolar motor by severing the common connection, wire 5, simply not supplying current. Once this is established the motor is now bipolar that can be driven by the low power driver that greatly reduces the number of cables used simplifying the cabling problem.

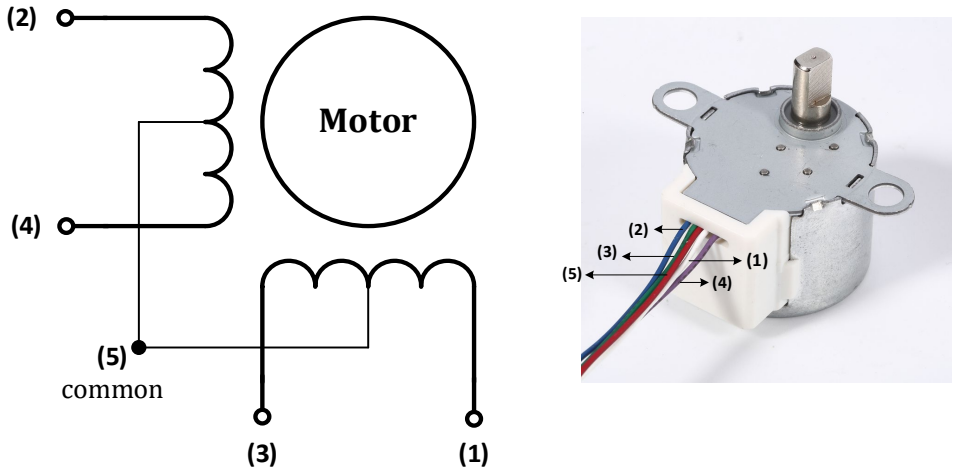

Figure C.2 Unipolar Motor Coil Connections

The motors are housed in a 3D printed bracket, held in its place by strong magnets and screws, as seen in Picture 12. This bracket is efficiently sized and designed to dispense food to the feeding holes of the fish tanks. The entire bracket will then be attached to the bars of the research system racks. As connections are established between the driver management and microcontroller, the microcontroller is connected to a Raspberry pi. A Raspberry pi (R-Pi) is a small-scale computer that is popular in internet of things-based projects as they come with a Wi-Fi compatible hardware. A software module designed to optimally monitored the feeding schedule is uploaded onto the R-Pi, that can be remotely accessible through the internet.

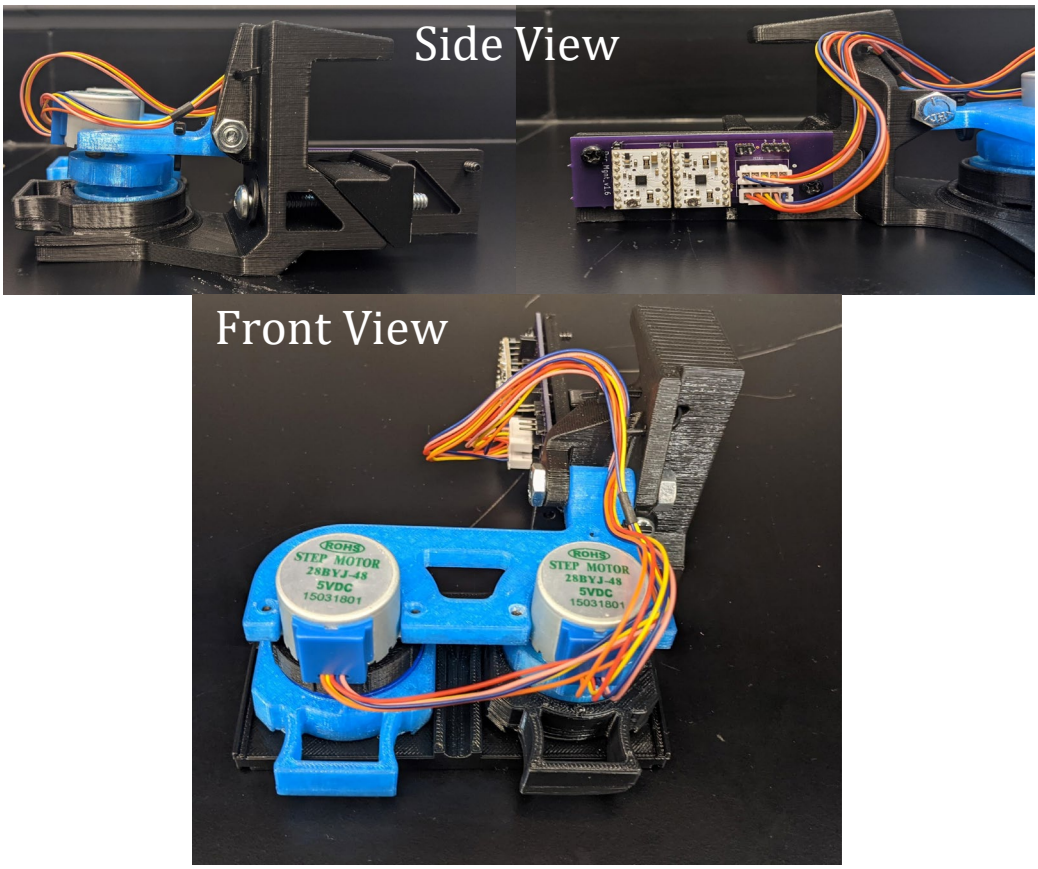

Picture C4 Feeding Bracket with Driver Management Board

Note that the time this appendix was being developed, the feeding system was still under design and modifications were being made.